REPORT DOCUMENTATION PAGE

Form Approved
OMB No. 0704-0188

1. REPORT DATE *(DD-MM-YYYY)*	2. REPORT TYPE	3. DATES COVERED *(From - To)*
08/01/2019	Final technical	1 Nov 2015 to 31 Oct 2018

4. TITLE AND SUBTITLE
Real-time dynamics of hot spots in microstructured energetic materials: experiments and simulations (Martin Schmidt)

5a. CONTRACT NUMBER

5b. GRANT NUMBER
FA9550-16-1-0042

5c. PROGRAM ELEMENT NUMBER

6. AUTHOR(S)
Dana D. Dlott, Priya Vashishta, Kenneth S. Suslick

5d. PROJECT NUMBER

5e. TASK NUMBER

5f. WORK UNIT NUMBER

7. PERFORMING ORGANIZATION NAME(S) AND ADDRESS(ES)
University of Illinois at Urbana-Champaign
Grants and Contracts Office
Champaign, IL 61820-6242

8. PERFORMING ORGANIZATION REPORT NUMBER

9. SPONSORING/MONITORING AGENCY NAME(S) AND ADDRESS(ES)
Air Force Office of Scientific Research
875 North Randolph Street, Suite 325
Arlington, VA 22203
Phone: 703-696-7797

10. SPONSOR/MONITOR'S ACRONYM(S)
AFOSR

11. SPONSOR/MONITOR'S REPORT NUMBER(S)

12. DISTRIBUTION/AVAILABILITY STATEMENT
Approved for Public Release, Distribution Unlimited

13. SUPPLEMENTARY NOTES

14. ABSTRACT
This project was a joint experimental/theoretical study of how microstructure affects energetic material initiation. Experiments were performed to study initiation by frictional rubbing, low velocity impact and high velocity impact on a variety of plastic-bonded explosives and single crystals. Theoretical modeling with multimillion atom simulations was used to explain the sensitivity of explosives to rubbing along different crystallographic axes and to explain the high temperatures observed at short times in shocked explosives.

15. SUBJECT TERMS
Energetic materials, shock waves, atomistic simulations, thermal imaging, microstructure, initiation, detonation

16. SECURITY CLASSIFICATION OF:			17. LIMITATION OF ABSTRACT	18. NUMBER OF PAGES	19a. NAME OF RESPONSIBLE PERSON
a. REPORT	b. ABSTRACT	c. THIS PAGE			Dana D Dlott
					19b. TELEPHONE NUMBER *(Include area code)*
A	A	A	A	31	217-333-3574

INSTRUCTIONS FOR COMPLETING SF 298

1. REPORT DATE. Full publication date, including day, month, if available. Must cite at least the year and be Year 2000 compliant, e.g. 30-06-1998; xx-06-1998; xx-xx-1998.

2. REPORT TYPE. State the type of report, such as final, technical, interim, memorandum, master's thesis, progress, quarterly, research, special, group study, etc.

3. DATE COVERED. Indicate the time during which the work was performed and the report was written, e.g., Jun 1997 - Jun 1998; 1-10 Jun 1996; May - Nov 1998; Nov 1998.

4. TITLE. Enter title and subtitle with volume number and part number, if applicable. On classified documents, enter the title classification in parentheses.

5a. CONTRACT NUMBER. Enter all contract numbers as they appear in the report, e.g. F33315-86-C-5169.

5b. GRANT NUMBER. Enter all grant numbers as they appear in the report. e.g. AFOSR-82-1234.

5c. PROGRAM ELEMENT NUMBER. Enter all program element numbers as they appear in the report, e.g. 61101A.

5e. TASK NUMBER. Enter all task numbers as they appear in the report, e.g. 05; RF0330201; T4112.

5f. WORK UNIT NUMBER. Enter all work unit numbers as they appear in the report, e.g. 001; AFAPL30480105.

6. AUTHOR(S). Enter name(s) of person(s) responsible for writing the report, performing the research, or credited with the content of the report. The form of entry is the last name, first name, middle initial, and additional qualifiers separated by commas, e.g. Smith, Richard, J, Jr.

7. PERFORMING ORGANIZATION NAME(S) AND ADDRESS(ES). Self-explanatory.

8. PERFORMING ORGANIZATION REPORT NUMBER. Enter all unique alphanumeric report numbers assigned by the performing organization, e.g. BRL-1234; AFWL-TR-85-4017-Vol-21-PT-2.

9. SPONSORING/MONITORING AGENCY NAME(S) AND ADDRESS(ES). Enter the name and address of the organization(s) financially responsible for and monitoring the work.

10. SPONSOR/MONITOR'S ACRONYM(S). Enter, if available, e.g. BRL, ARDEC, NADC.

11. SPONSOR/MONITOR'S REPORT NUMBER(S). Enter report number as assigned by the sponsoring/ monitoring agency, if available, e.g. BRL-TR-829; -215.

12. DISTRIBUTION/AVAILABILITY STATEMENT. Use agency-mandated availability statements to indicate the public availability or distribution limitations of the report. If additional limitations/ restrictions or special markings are indicated, follow agency authorization procedures, e.g. RD/FRD, PROPIN, ITAR, etc. Include copyright information.

13. SUPPLEMENTARY NOTES. Enter information not included elsewhere such as: prepared in cooperation with; translation of; report supersedes; old edition number, etc.

14. ABSTRACT. A brief (approximately 200 words) factual summary of the most significant information.

15. SUBJECT TERMS. Key words or phrases identifying major concepts in the report.

16. SECURITY CLASSIFICATION. Enter security classification in accordance with security classification regulations, e.g. U, C, S, etc. If this form contains classified information, stamp classification level on the top and bottom of this page.

17. LIMITATION OF ABSTRACT. This block must be completed to assign a distribution limitation to the abstract. Enter UU (Unclassified Unlimited) or SAR (Same as Report). An entry in this block is necessary if the abstract is to be limited.

Award FA9550-16-1-0042
1 Nov 2015 to 31 Oct 2018

"*Real-time dynamics of hot spots in microstructured energetic materials: experiments and simulations (Martin Schmidt)*"

Publications that acknowledge award FA9550-16-1-0042 during this reporting period

1. A. A. Banishev, W. L. Shaw, W. P. Bassett, and D. D. Dlott, High-speed laser-launched flyer impacts studied with ultrafast photography and velocimetry, J. Dyn. Behav. Mater. 2, 194-206 (2016). doi: 10.1007/s40870-016-0058-2
2. W. L. Shaw, "Reactive solids under shock compression, PhD thesis, University of Illinois, 2016.
3. W. P. Bassett and D. D. Dlott, High dynamic range emission measurements of shocked energetic materials: Octahydro-1,3,5,7-tetranitro-1,3,5,7-tetrazocine (HMX), J. Appl. Phys 119, 225103 (2016). doi: http://dx.doi.org/10.1063/1.4953353
4. W. P. Bassett and D. D. Dlott, Shock initiation of explosives: Temperature spikes and growth spurts, Appl. Phys. Lett. 109, 091903 (2016). doi: http://dx.doi.org/10.1063/1.4961619
5. W. P. Bassett and D. D. Dlott, Multichannel emission spectrometer for high dynamic range optical pyrometry of shock-driven materials, Rev. Sci. Instrum. 87, 103107 (2016). doi: http://dx.doi.org/10.1063/1.4964386
6. "Anisotropic frictional heating and defect generation in RDX molecular crystal", P. Rajak, A. Mishra, S. Tiwari, C. Sheng, R. K. Kalia, A. Nakano and P. Vashishta, Appl. Phy. Lett., 112, 211604 (2018).
7. "Shock compression of gas in silica nanopores", K. Nomura, P. Rajak, R. K. Kalia, A. Nakano and P. Vashishta, Applied Physics Letters, submitted.
8. "Time-dependent pressure distribution in microstructured shocked materials using fluorescent probe dyes", Alexandr Banishev, James M. Christensen and Dana D. Dlott, AIP Confer. Proc. 1793, 060010 (4 pages), (2017). doi: 10.1063/1.4971566
9. "32-Channel pyrometer with high dynamic range for studies of shocked nanothermites", Will P. Bassett and Dana D. Dlott, AIP Confer. Proc. 1793, 060012 (5 pages), (2017). doi: 10.1063/1.4971568.
10. "Shock compression dynamics under a microscope", Dana D. Dlott, AIP Confer. Proc. 1793, 020001 (9 pages), (2017) doi: 10.1063/1.4971568.
11. "Shock initiation of explosives: High temperature hot spots explained", Will P. Bassett, Belinda Johnson, Nitin K. Neelakantan, Kenneth S. Suslick and Dana D. Dlott, Appl. Phys. Lett. 111, 061902 (2017). doi: 10.1063/1.4985593.
12. "Shock compression spectroscopy under a microscope", Dana D. Dlott, Proceedings of International Symposium on Shock Waves 31, Nagoya, Japan (in press).
13. "Shock compression spectroscopy of quantum dots", James Christensen, Alexandr Banishev and Dana D. Dlott, Proceedings of 20th Biennial APS Conference on Shock Compression of Condensed Matter, in press 2017.
14. "Numerical predictions of shock propagation through unreactive and reactive liquids with experiment validation", Svjetlana Stekovic, Erin Nissen, Mithun Bhowmick, D. Scott Stewart, Dana D. Dlott, Proceedings of 20th Biennial APS Conference on Shock Compression of Condensed Matter, in press 2017.
15. "Functionalized silicone composites: omniphobic coatings, microspheres and plastic explosives", Nitin Neelakantan PhD Thesis, University of Illinois at Urbana-Champaign, 2017.

16. “Shock Initiation of Explosives Under the Microscope”, Will P. Bassett, PhD Thesis, University of Illinois at Urbana-Champaign, 2018.
17. “Thermal explosions of polymer-bonded explosives with high time and space resolution”, Zhiwei Men, Kenneth S. Suslick and Dana D. Dlott, J. Phys. Chem. C, 122, pp. 14289-14295 (2018).
18. “Detonation on a tabletop: nitromethane with high time and space resolution”, Mithun Bhowmick, Erin Nissen and Dana D. Dlott, J. Appl. Phys. 7, 075901 (2018).
19. “Sub-detonative and detonative dynamics in PETN-based polymer-bound explosives under nanosecond shock conditions”, Will P. Bassett, Belinda P. Johnson, Lawrence Salvati and Dana D. Dlott, Proc. Inter. Detonation Symp, 2018 (submitted).
20. “Optical windows as materials for high-speed shock wave detectors”, Mithun Bhowmick, Will P. Bassett, Sergey Matveev, Lawrence Salvati III and Dana D. Dlott, AIP Advances 8, 125123 (2018).
21. 1. Z. Men, W. P. Bassett, K. S. Suslick, and D. D. Dlott, Drop hammer with high-speed thermal imaging, Rev. Sci. Instrumen. 89, 115104 (2018).
22. Jordan J. Hinman, “Control of micro- and nanostructure: I. Polymer gas chromatograhy microcolumns and II Applications of Ultrasound, Ph.D. Thesis, University of Illinois, 2018.

People working on the grant UIUC = University of Illinois at Urbana-Champaign, USC CACS = University of Southern California Collaboratory for Advanced Computing and Simulations

Dana D. Dlott (UIUC), PI
Kenneth S. Suslick (UIUC), co-PI
Priya Vashishta (USC CACS), co-PI
Rajiv Kalia (USC CACS), co-PI
Ken-Ichi Nomura (USC CACS)
Alexandr A. Banishev (UIUC), postdoc, now at IPG Photonics
Zhiwei Men (UIUC), visiting scholar (China)
William L. Shaw (UIUC), now Ph.D. staff at Lawrence Livermore National Laboratory.
Will P. Bassett (UIUC), now Ph.D. staff at Lawrence Livermore National Laboratory.
Nithin Neelakantan (UIUC)
Pankaj Rajak (USC CACS)
Subodh Tiwari, (USC CACS)
Jordan Hinman (UIUC),
Belinda Johnson (UIUC), graduate student
Ankit Mishra (USC), graduate student
Tom Linker (USC), graduate student
Ruru Ma (USC), graduate student

Collaborations and transitions

We have worked to transition parts of the shock compression microscope to Los Alamos (Kathryn Brown), Army Research Laboratory (Steven Dean) and Sandia (Alex Tappan). we have collaborated with Dr. Lara Leininger of Livermore on TATB measurements. We collaborate with Scott Stewart (AFRL) and Keo Springer (LLNL) on ALE3D simulations.

Accomplishments

Background. The goal of this project was to understand dynamic material interactions, specifically the effects of microstructure on energetic material (EM) initiation, by seamlessly connecting experiments with atomistic simulations. The project was a collaborative effort between , Dlott and Suslick at UIUC, and Kalia and Vashishta at USC. The effort consisted of development of techniques to produce and characterize EM with controlled composition and architecture (Suslick, Dlott), techniques to understand EM initiation by low velocity impacts from a highly-instrumented drop hammer (Dlott, Suslick), techniques to understand EM initiation by friction provided by ultrasound (Dlott, Suslick, Vashishta), and techniques to understand EM initiation provided by high-velocity impacts (Dlott, Vashishta).

Our team has developed the ability to produce a variety of plastic-bonded explosive (PBX) formulations, including PBX that closely mimic some commercially-available explosives, and simplified model architectures based on single explosive crystal in a polymer matrix decorated with other explosive particles or nanoparticles. We characterize these formulations using scanning electron microscopy (SEM) and energy-resolved SEM, which lets us image the explosives and binder separately, and micro and nano x-ray computed tomography (CT).

We have built a drop-hammer[1] that includes video rate thermal imaging and high-speed thermal imaging. These imagers measure the spatial distribution of temperatures with 15 μm spatial and 1 μs temporal resolutions of samples impacted by the hammer.[2-4] The performance of the drop hammer was demonstrated with PBX samples. Then the drop hammer was transported to the Vikas Tomar lab at Purdue, where we will collaborate on energetic material initiation and some new projects such as understanding how impacts set lithium batteries afire.

We have shown we can initiate polymer-bonded EM by high-speed rubbing using a 20 kHz ultrasonic horn equipped with the same kinds of high-speed thermal imagers.[2-5] Significantly, we have shown we can control where the heat is input to the explosive by painting the surface to be heated with a small amount of lubricant.[5] We measured the time dependence of thermal explosions in polymer-bonded RDX and HMX.[2] The USC group has done atomistic simulations of frictional rubbing of RDX,[6] and they made clear predictions about which directions rubbing would produce the most rapid initiation. Following these calculations, the UIUC group designed an ultrasound system to study initiation of RDX crystals in the orientations specified by USC and found good agreement between the atomistic simulations and the ultrasound experiments.

The UIUC group developed the "shock compression microscope"[7] that allows us to study EM with high-speed impacts in the 0.5-6 km/s range, using a wide range of high-speed optical and optomechanical diagnostics that measure pressure, density, temperature, microstructure and composition on the nanosecond time scale. We have fabricated cassettes with about 200 tiny PBX charges that we can shock initiate in a controlled manner.[8-10] We have shown that we can produce well-characterized detonations in homogeneous[11] and plastic-bonded explosives. We have used optical pyrometry and high-speed imaging to study the production and growth of hot spots in shocked EM.[10] A very interesting observation was the ubiquity of hot spots produced by gas compression in nanopores.[10] The USC group has done simulations of shocked nanopores in explosives with and without gas fill and reported computed temperatures that closely matched the UIUC shock experiments.

Preparation and characterization of PBX materials with controlled architectures.

We have developed some simple methods for mass-producing disposable arrays of tiny PBX charges. An array might have 200 charges, each 1 mm in diameter with a thickness in the 25-250 μm range. We sieve the particles to size them and mix them with binder and other additives. We have mostly used silicone rubber (PDMS) as the binder, but we have begun producing explosives with HTPB binders as well. Before the binder cures, we run the explosive through a hydraulic press to squeeze out the voids. This is crucial to minimize hot spots.[10] We have routinely achieved a void density of 1% or less. Figure 1 shows a photo of an array of 1 mm charges of XTX-8003,[12] which is 80% PETN and 20% PDMS. Also in Fig. 4 are an x-ray CT scan, an SEM and a particle size distribution. You can see the voids in the CT scan (Fig. 4c), and there are not many and they are small. We are working on advanced characterization techniques such as scanning energy-dispersed x-ray spectroscopy microscopy. With energy dispersion we can resolve the nitrogen in the PETN and the silicon in the PDMS. Figure 2 shows the PETN in red and the PDMS in green.

We have also developed disposable mass-produced arrays of about 50 tiny optical cuvettes which we can use for liquid explosives such as the nitromethane experiments described below.[11] The key is to use a 9 μm thick Al foil lid which is flexible enough to seal the liquid inside the cuvette and thin enough to transmit most of the impact energy from the flyer plate.

One of the problems in studying microstructural effects is how to characterize the microstructure. We do not know how to make a series of samples where the microstructure runs from zero to one. We are approaching this problem using the "system-bath" model that is widely used in statistical mechanics. Here the "system" is a larger grain of the explosive, let's say 50 μm. The "grain" could be a single crystal or it could be the kind of defective aggregates used in practical explosives. The bath is the surrounding polymer matrix plus whatever powders we add to it. We can try to understand how individual grains surrounded by polymer behave upon impact, and we can feed different amounts of reactive or inert particles into the surroundings to see how that affects the system grain.

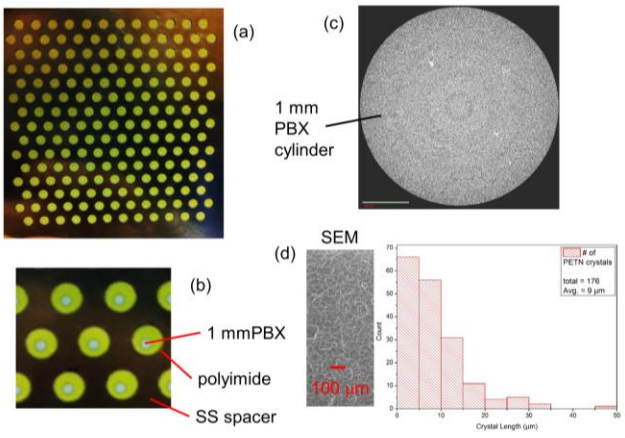

Fig. 1. A two inch array containing 186 1 mm diameter charges of XTX8003, which is 80% PETN and 20% PDMS binder.

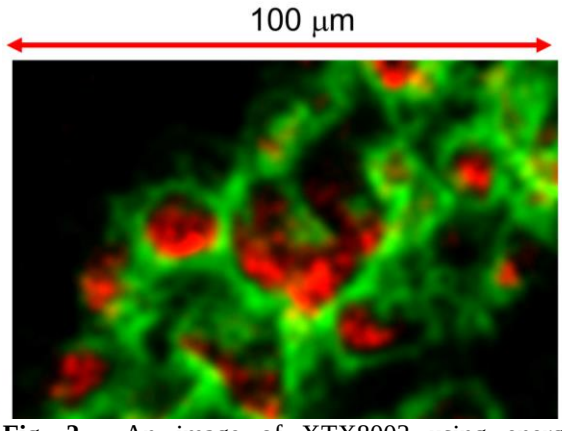

Fig. 2. An image of XTX8003 using energy dispersive x-ray spectroscopy microscopy. The red regions contain N-atoms and the green regions Si-atoms. The red is PETN and the green is silicone rubber.

So far we have looked at single grains of PETN encased in a polymer, as shown in Fig. 3. We have developed methods to produce many tens of single crystals with slow evaporation, but right now we are looking at the really messy crystals and crystal aggregates produced by rapid precipitation. These, we believe, are more representative of what is in real explosives. One can see there are a lot of different morphologies. These are single snapshots taken with a 5 ns integration window during the first 5 ns of impact with a 2.5 km/s flyer plate. The yellow regions are regions where the PETN is hot enough to emit >2000K thermal radiation. We are amazed at the hot spot structures seen in these images and the level of detail we can see. We have recently been able to borrow a high speed camera from Livermore which gives us four frames per shot. With this camera we get continuity of hot spot development, as shown in Fig. 4.

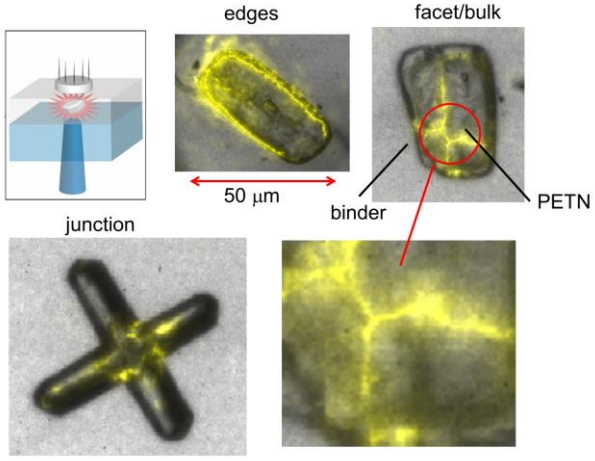

Fig. 3. 5 ns snapshots of PETN crystals encased in polymer binder impacted by a 2.5 km/s flyer plate. The bright regions are emitting thermal radiation of 3000K or

Figure 5 shows some characteristically different hot spot patterns that are concentrated at either the edges, on a facet (or perhaps below it in the bulk) and at crystal junctions. We have the ability to focus our optical pyrometer down to less than 50 μm spot size,[13] so we can actually measure the temperature histories at different locations, as shown in Fig. 5. There is a variable aperture in the pyrometer, so we can translate the sample around and select the region of interest. Figure 5 shows that edges, faces and junctions have different temperatures and time-dependent temperature profiles, and these differences seem to be not random. A big surprise to us was that we actually get characteristically different behavior from edges, facets and junctions. Figure 5 shows that edges reach their maximum temperature at about 30 ns. The facets, by contrast, seem to reach their maximum temperature around 60 ns. The crystal

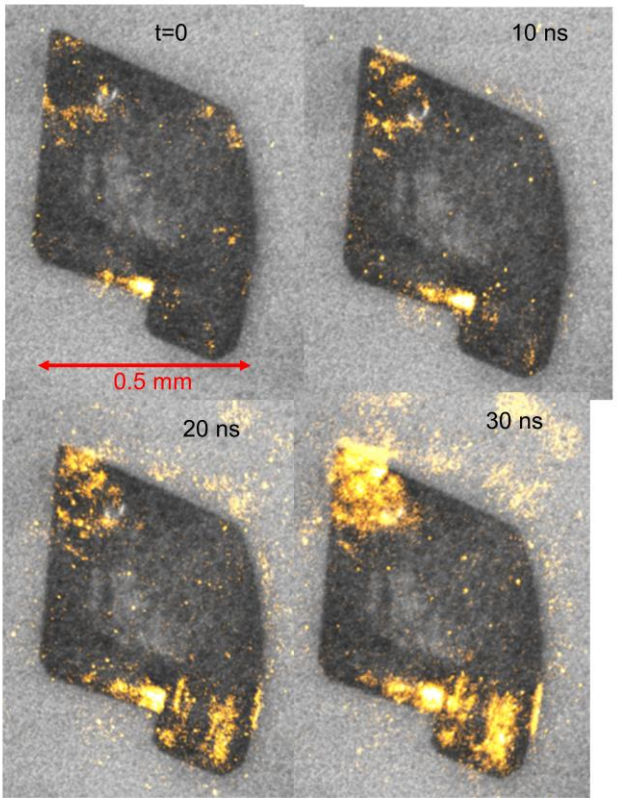

Fig. 4. HMX crystal embedded in PDMS with 2 km/s impact shows the generation and subsequent development of hot spots using 4-frame camera from Livermore.

junctions reach the highest temperatures in the shortest times.

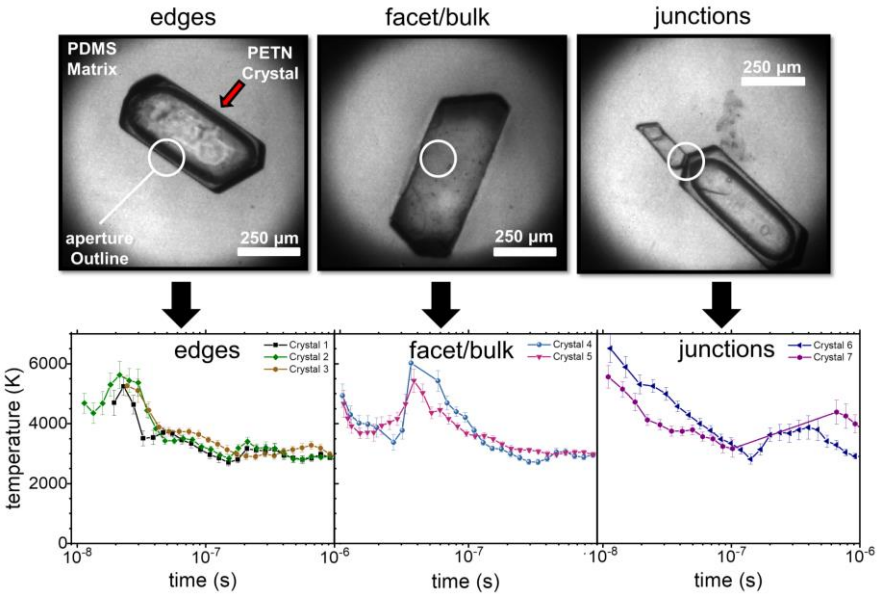

Fig. 5. Temperature histories of polymer-encased PETN crystals obtained by selecting the region (white circle) observed by the optical pyrometer. Temperature histories are characteristically different at edges, facets and junctions.

Low velocity impact initiation with thermal imaging drop hammer

The drop hammer test is the easiest way to assess the sensitivity of explosive materials, but drop hammer results for low-velocity impacts have not been able to explain how explosives will react to other kinds of initiating stimuli. In order to do that, we have to understand the fundamental mechanisms of drop hammer initiation and how they differ from other initiation methods. For this reason, there is interest in instrumented drop hammers that help reveal what the drop hammer does at a fundamental level. We have developed a drop hammer that combines two types of mid-wavelength infrared (MWIR) imagers that, when operated simultaneously, can detect both the rapid explosion and slower combustion from impact-initiated polymer-bonded explosives with high time (1 µs) and space (15 µm) resolution.[1] Results were presented that show how to vibration isolate the drop hammer to minimize MWIR image shaking during impact and to quantify the noise floor for MWIR temperature determinations via optical pyrometry. Experiments were performed on polymer-encased crystals of RDX ($[CH_2\text{-}NNO_2]_3$) and HMX ($[CH_2\text{-}NNO_2]_4$). Our experiments showed that drop-hammer initiated explosions occur in two phases with roughly 100 µs between explosions. Drop-hammer initiation is compared to an ultrasonic hammer, which initiates explosions by rapid frictional rubbing of the explosive surfaces against the surrounding polymer. The explosion rise time is faster with the drop hammer because the drop hammer inputs energy

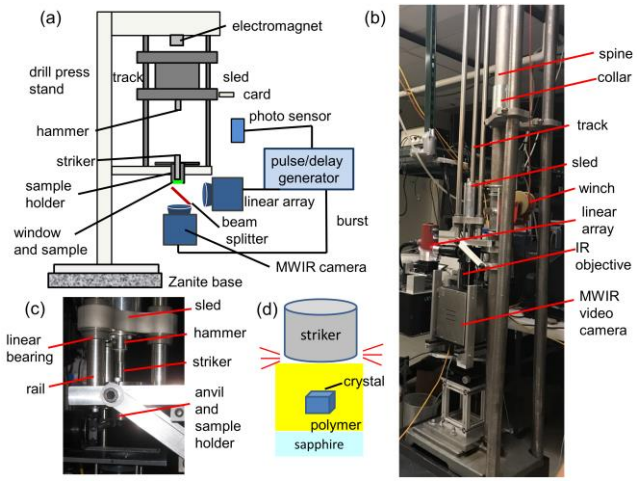

Fig. 6. (a) Schematic of drop hammer with dual thermal imagers. (b) Photo of drop hammer. MWIR = mid-wavelength infrared. (c) Close up of the sled showing the rail, striker and anvil. (d) Schematic of striker impacting polymer-encased crystal.

throughout the explosive volume, whereas the ultrasonic hammer produces localized heating and much more heat at the explosive surface.[1]

No individual thermal imaging detector can, at this time, provide both high spatial resolution images and high time resolution. We have found this difficulty can be overcome by simultaneously observing the sample with two different kinds of thermal imaging detectors.[2] We previously showed how this combination[2] could be used to observe the dynamics of energetic materials initiated by an ultrasonic hammer.[2,3,5] Here we have incorporated this detector combination into a drop hammer. One detector is a thermal imaging video camera which provides 640 x 512 MCT detector elements (327,680 pixels) with optics that provide near-diffraction limited spatial resolution of about 15 μm.[2-5] Although this video camera provides excellent high-resolution images, unfortunately its 8.3 ms interframe interval, which is limited by the need to readout 327,680 pixels with a single analog-to-digital converter, is too slow to time resolve the explosion.[2] The second detector was a 32 x 1 linear array of MCT detector elements. The MCT elements have a nominal risetime of 1 μs, and each element has its own 4 MHz analog-to-digital converter.[2] Using the 32 high-speed analog-to-digital converters, the overall time response is about 1 μs and the linear array produces 4 million line-scan images per second. The linear array captures thermal emission over a smaller field of view than the camera, but it gives the temperature, via single-color pyrometry, at 32 points along a line running through the explosion. The time resolution of the linear array is 33,000 times faster than the video camera. The complementary video camera and linear array thermal imagers produce both high-resolution images with relatively poor time resolution combined with lower-resolution images with far greater time resolution.[2]

The drop hammer, shown in Fig. 6 in schematic (Fig. 6a) and photographic (Figs. 6b-c) forms, has a weight sled with an adjustable drop height and weight. The drop hammer has an electromagnetic trigger to initiate the sled drop. The falling sled triggers an optical sensor to synchronize the impact with the two fast IR imagers. The drop hammer has vibration isolation to protect surrounding instruments. It is designed to mount the imagers close enough to the sample (Fig. 6a,b) to obtain near diffraction-limited spatial resolution (15 μm) in the MWIR. The impact with the striker causes the images to shake, and efforts were made to characterize and minimize image shaking.

The drop hammer is built around a surplus drill press stand. The stand has a cast iron 15" × 20" base plate with a 4' long 3" OD cast iron pipe with 1/8" thick walls. This pipe, which formed the "spine" of the drop hammer (Fig. 1b) was extended to 95" with a stainless steel (304-SS) pipe with the same OD and wall thickness using a custom-made collar shown in Fig. 1b. The original drill press version of the drop hammer caused nearby equipment, especially our mode-locked femtosecond lasers, to malfunction when the hammer was dropped, so the drill press was mounted on a 6" thick vibration isolation base plate made from a Zanite Plus polymer-concrete composite (BaseTek LLC) known for its vibration isolation properties. The Zanite Plus base plate had threaded ½-13 inserts to bolt it to the drill press and to mount five vibration controlling leveling pads (J. W. Winco #16NSNS) to the underside.

The weight sled (Figs. 6b,c) has three linear bearings (McMaster-Carr) that ride along a triangular track of three 1" diameter case-harden 303 stainless steel guide rails 1.0000 ± 0.0005"

diameter with 0.002”/ft straightness (Nordex) (Fig. 6c). The ends of the rods were drilled and tapped to accept ¼-20 socket-head screws that bolted the rods to the sample holder. The sled carried a stack of 0.5 kg lead weights, and the load could be varied from 0.5 to 4.5 kg.

An end plate mounted on a carrier could be moved along the track to adjust the drop height above the sample from 1” to 40”. Assuming a frictionless drop under the acceleration of terrestrial gravity, the impact velocity can range from 0.25 m/s to 10 m/s. The end plate had a 12V DC, 4.4 W electromagnet with a carrying capacity of 22.6 kg (McMaster-Carr). The top plate of the sled was magnetic iron that could be held by the electromagnet when it was engaged. The electromagnet is controlled by an AC to DC electromagnet transformer (McMaster-Carr) with a manual control switch which can reverse current to launch the sled. By varying the height and weight of the sled, the kinetic energy of impact could be varied from 0.015J to 225J.

The sled had a card that passed through a photosensor to generate a fast electronic pulse with a 5 μs rise time, used to trigger a digital delay generator (Stanford Research Systems DG645) which controlled the MWIR cameras. Time $t = 0$ is defined by the trigger pulse, but the trigger pulse was generated when the striker was about 30 mm above the sample. The actual impact occurred at an instant in time that varied with the height of the drop, but which was in the 5-10 ms range.

The hammer was a 0.5000 ± 0.0001” pin gauge made of tool steel with a hardness of C60 on the Rockwell scale (McMaster-Carr). The hammer drives an identical striking pin into the test sample. The striker and hammer pins (Figs. 6c-d) are frequently damaged but easy and inexpensive to replace. The anvils were sapphire windows 15 mm diameter and 4 mm thick (Thorlabs). These anvils were transparent in the MWIR region and thick enough to have good survivability to maintain integrity during the thermal imaging measurements.

For MWIR imaging, we obtained near diffraction-limited resolution of about 15 μm using a matched pair of 1X MWIR microscope objectives having N.A. = 0.22 (Asio 1X, Janos Tech, Keene, NH).[3,4] The video camera (IRE-640M, Sofradir-EC Inc.) had 15-μm pitch 640×512 MCT detector elements cooled to 90K, and a cooled prefilter that transmitted light only in the MWIR 3.7–4.8 μm range. The maximum video rate was 120 Hz (8.33 ms). The camera was used as a single-color pyrometer, as discussed previously.[7] Single-color pyrometry determines the temperature from the absolute emission intensity integrated over a specific known spectral range, so in order to obtain the temperature, the emissivity must also be known. We used a calibrated blackbody standard (IR-508, Infrared Systems Development) and measured the temperature dependence of RDX crystal emissivity with crystals and binders in a thermostated oven.[3] Due to the close similarity in chemical structure and optical properties of RDX and HMX, we assumed the measured RDX emissivity for HMX. The linear array detector (TEDAS-3200, Infrared Systems Development Corp., Winter Park, FL) was liquid N_2 cooled. Its 0.1 mm 32 MCT detector elements with 0.112 mm pitch and cooled optical prefilter were designed by the manufacturer to closely match the spectral response of the video camera, so we used the same emissivity calibration as with the video camera.

The camera and the linear array viewed the sample through a 50:50 MWIR beamsplitter coated on a 50 mm diameter ZnSe substrate 3 mm thick (Spectral Systems, Hopewell Junction,

NY). The working distance from objective to sample was 60 mm. As shown in Fig. 6b, the linear array was mounted on a laser table adjacent to the drop hammer while the camera was mounted on the drop hammer itself. Mounting the camera on the drop hammer reduced image shaking, since the sample and the camera experienced similar correlated vibrational histories. Image shaking was not a significant problem for the linear array, since it already has lower spatial resolution and is looking at fast processes where there is not enough time for much shaking to occur. Both detectors were mounted on *xyz* translation stages to align the images and focus the objectives.

Here we present representative results obtained from a smaller (0.5 mm) and a larger (1 mm) RDX crystal and a larger (1 mm) HMX crystal, initially at 300K, using the maximum drop height of 40" and the maximum drop energy of 225J. MWIR video images for the 0.5 mm polymer-encased RDX crystal with a 225J drop from 40" are shown in Figs. 7 and 8, where time = 0 denotes a time that precedes the impact by a few milliseconds. In Fig. 7, the MWIR images were acquired with the video camera at 10 ms intervals. The crystal temperature peaked at 10 ms, where it appeared to be about 400K. However, the 10 ms interframe time is too short to time resolve the actual crystal explosion, so the image Fig. 7b does not represent the actual peak temperature; rather it represents the single-color pyrometry effective temperature of the explosion derived from the MWIR intensity averaged over the 10 ms camera acquisition window.[2] Figure 7 also shows the sample stays warm for many tens of milliseconds after the explosion.

Figure 8 shows line-out images from the smaller 0.5 mm RDX crystal acquired simultaneously with the video in Fig. 7, using the much faster linear array detector. Figure 8a shows an apparently instantaneous temperature burst to about 1000K peak occurring at about 4.8 ms, followed by a much slower, lower-temperature burn. An expanded time version of the linear array output in Fig. 8b shows the RDX crystal explosion lasted approximately 150 μs, and the

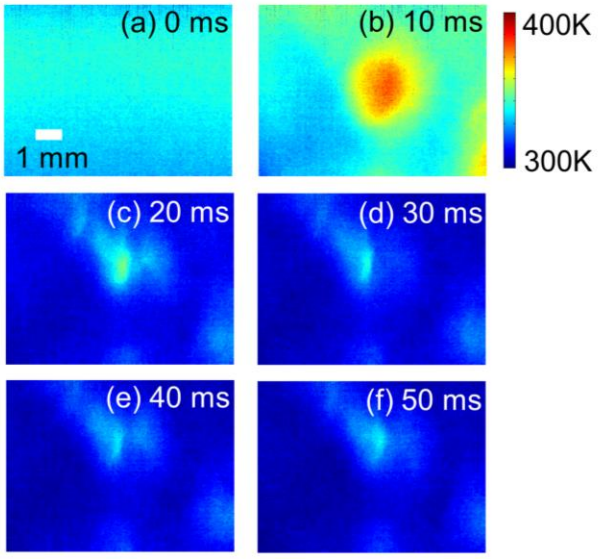

Fig. 7. Selected video images at 10 ms intervals from a 40" impact with a polymer-encased 0.5 mm RDX crystal.

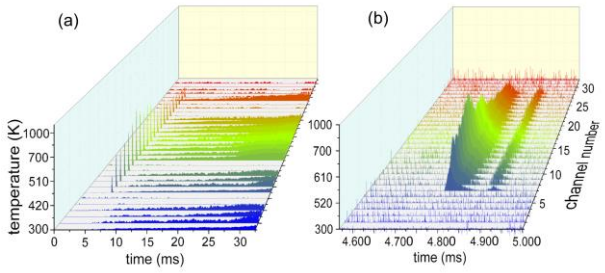

Fig. 8. Output of the linear MWIR array during a 40" drop impact with the polymer-encased 0.5 mm RDX crystal, obtained simultaneously with the video images in Fig. 5. The linear array is measuring the temperature in a strip 0.5 mm wide running through the middle of the crystal. (a) The full 32 ms record shows an instantaneous fast explosion at about 5 ms and a much slower burning lasting many tens of milliseconds. (b) Same record on an expanded scale showing the two-part explosion.

main explosion was followed by a second, weaker explosion about 100 μs later.

Figures 9 and 10 show the same type of measurement on a larger 1 mm polymer-encased RDX crystal, again with a 225J drop from 40". This larger crystal has about ten times the volume of the crystal used for Figs. 7 and 8, and the explosion was much more violent. As shown in Fig. 7b, the camera recorded a peak temperature of about 600K, and again the sample stayed warm for many tens of milliseconds. The linear array data in Fig. 10a shows the explosion temperature peak was actually about 1500K. Figure 10b shows that the RDX explosion occurred in two stages, but the second stage appeared sooner and was hotter than with the smaller RDX crystal.

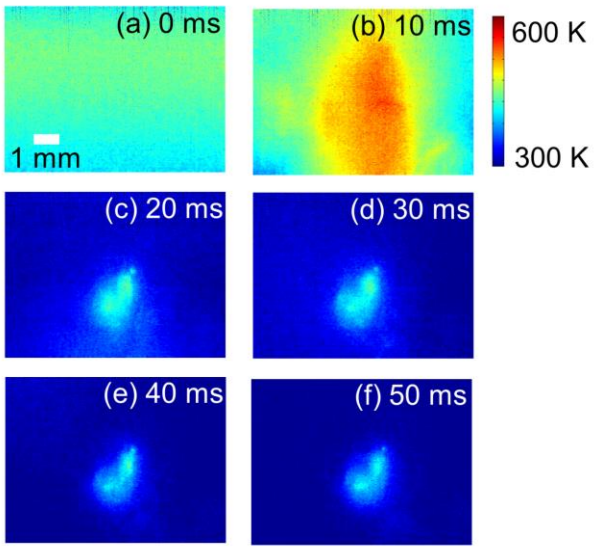

Fig. 9. Selected video images at 10 ms intervals from a 40" impact with a polymer-encased 1 mm RDX crystal.

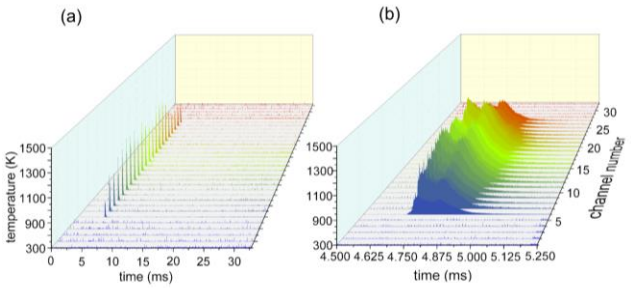

Fig. 10. Output of the linear MWIR array with a 40" impact with the polymer-encased 1 mm RDX crystal. (a) The full 32 ms record. (b) Same record on an expanded scale showing the two-part explosion.

Figures 11 and 12 show results from a polymer-encased 1 mm HMX crystal with a 225J drop from 40" (1.02 m). The video camera results in Fig. 11 show an explosion at 10 ms (Fig. 11b)which was much more violent and widespread than with RDX, which is consistent with HMX being the higher-performance explosive. There was not much warm material remaining after the big explosion, which suggests the HMX explosion more completely consumed the energetic material. The linear array results in Fig. 12 show an intense 2-stage explosion starting at about 5.3 ms and reaching a peak temperature of about 3000K. Figure 12b shows that the second stage of the HMX explosion was hotter than the first, unlike the RDX explosions.

Figure 13a,c compare time-dependent temperature profiles for drop-hammer experiments on RDX and HMX. These profiles are the time-dependent temperature average within a strip 0.3 mm wide running through the hottest part of the crystal explosions shown in Figs. 8b, 10b and 12b, and each displayed temperature is the average over a 5 μs time window.[2] Each time axis in the panels of Fig. 13 has an arbitrary time shift accounting for variable dead times, to put the explosion in the center of the panel. The time shift was about 5 ms for the drop hammer and a few tens of milliseconds for the ultrasound.

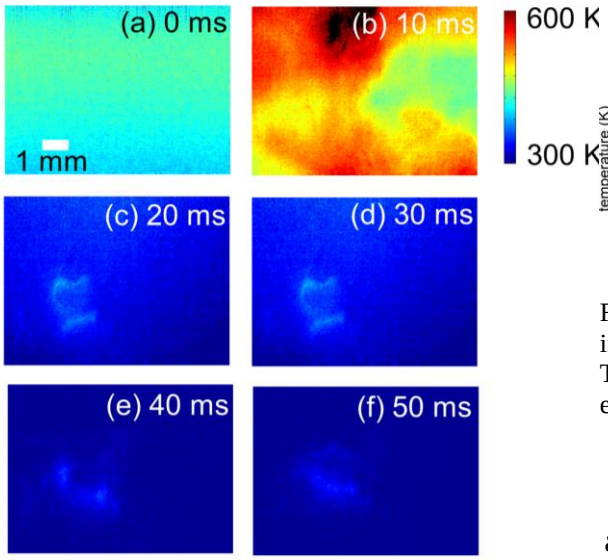

Fig. 11. Selected MWIR video images at 10 ms intervals from a 40" impact with a polymer-encased 1 mm HMX crystal.

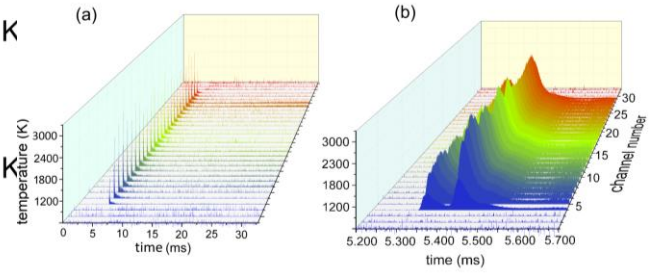

Fig. 12. Output of the linear MWIR array during a 40" impact with polymer-encased 1 mm HMX crystal. (a) The full 32 ms record. (b) Same record on an expanded scale showing the two-part explosion.

13a), the first explosion had a rise time of 10 μs and the second, much lower temperature explosion was about 150 μs after the first. With the larger RDX crystal (Fig. 13a), the first explosion was much hotter than with the smaller crystal, and it had a rise time of 15 μs. The second explosion was about 90 μs after the first.

With the HMX crystal, Fig. 13b shows there was also a two-phase explosion. Both phases had rise times of about 10 μs. The second, more intense explosion was about 90 μs after the first.

In Figs. 13-15 we compare drop hammer initiation of RDX and HMX crystals to initiation of similarly-sized RDX and HMX crystals using high-speed (20 kHz) frictional rubbing produced by the ultrasonic hammer. Figures 14 and 15 show the linear array output during the explosion phase for the larger RDX and HMX crystals, respectively. With ultrasound initiation, the rise times are

The temperature rise times (the approximate time interval between the 10% and 90% of the temperature peak) in Figs. 13a,b were quite a bit slower than the instrument time resolution of 1 μs, so the linear array has accurately determined these rise times. With the smaller RDX crystal (Fig.

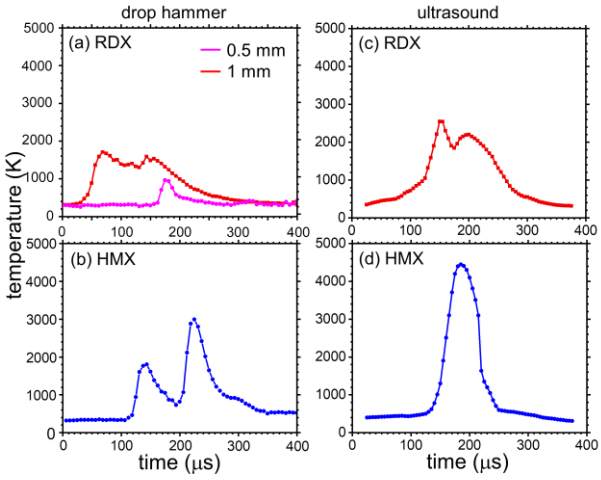

Fig. 13. Comparison of time-dependent temperature profiles for polymer-encased RDX and HMX crystals with a 40" drop with crystals initiated by fast rubbing with an ultrasonic hammer. These are the temperatures from a 0.5 mm wide strip at the center of the crystals. (a) Smaller 0.5 mm and larger 1 mm RDX crystal with drop hammer. (b) A 1 mm HMX crystal with drop hammer. (c) A 1 mm RDX crystal with ultrasonic hammer. (d) A 1 mm HMX crystal with ultrasonic hammer. All the panels have an arbitrary time shift to locate the fast explosion in the center of the panel. This shift is about 5 ms for drop hammer and a few tens of milliseconds for the ultrasonic hammer.

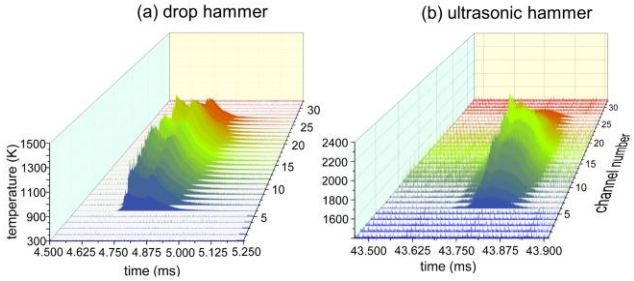

Fig. 14. Comparison of thermal profiles for a 1 mm RDX crystal (a) with a 40" drop from the drop hammer or (b) initiation using the ultrasonic hammer.

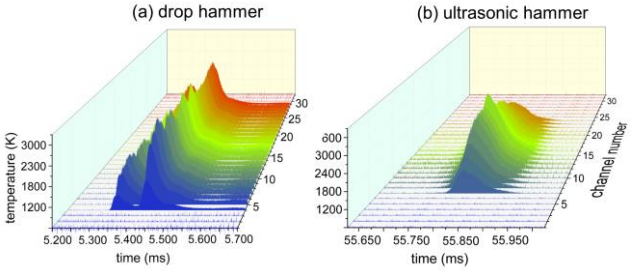

Fig. 15. Comparison of thermal profiles for a 1 mm HMX crystal (a) with a 40" drop from the drop hammer or (b) initiation using the ultrasonic hammer.

considerably slower than with the drop hammer, 40-60 μs compared to the 10-20 μs obtained with drop hammer. The peak temperatures, however, are considerably higher with ultrasound. With both ultrasound and drop hammer initiation, RDX has a two-part explosion. With drop hammer HMX had a two-part explosion but with ultrasound HMX had a single-part explosion.

Two factors that limit the accuracy of high-speed thermal imaging measurements on impacted materials are image shaking and the spurious MWIR light produced by the drop-hammer components themselves. We greatly reduced shaking by mounting the video camera directly to the drop hammer, and in this configuration the shaking, at its present level, has no effect on our ability to measure the fast explosion with high spatial resolution. The fast explosion occurs a few milliseconds after trigger, and according to Figs. 13-15 it typically lasts 200-300 μs.

The thermal profiles for impact-initiated RDX and HMX all have a two-part fast explosion. With the smaller RDX crystal, the interval between the two parts was about 150 μs, and with the larger RDX or HMX crystals, this interval was 90 μs. This raises the question as to whether the two-part explosion is an consequence of the experimental design or an intrinsic process due to thermomechanical kinetics of the explosives. If the former, it would most likely be due to the way the striker bounces[14] when it impacts the sample. The bouncing causes the loading of the sample to have an oscillatory component after the initial compression.[14] The striker velocity in our experiments was about 10 m/s and the size of the explosive targets were on the order of 0.5-1.0 mm. In the roughly 100 μs interval between explosions, the striker could move about 1 mm, which is comparable to the sample dimensions, so this argument cannot rule out the possibility that the two-part explosions result from the way the striker bounces off the target. However the time interval between explosions, 150 μs, was quite different for the smaller RDX crystal than for the larger RDX and HMX crystals, where it was 90 μs. Williamson and co-workers[15] detected similar two-part emission bursts from HMX powder in a drop hammer with about one-half the impact velocity used here. The fact that this time interval was similar with two quite different drop hammer instruments, and that the time intervals were significantly different in our apparatus using different sample materials suggests the two-part explosion is indeed a property of the impacted explosive.

In comparing the drop hammer to a quite different initiation method, the ultrasonic hammer, the fast explosion temperature profiles in Figure 13 had similar durations of 100-200

μs. However the temperature rise time was quite a bit faster with the drop hammer and the peak temperatures were quite a bit greater with ultrasound. This admittedly small set of results seems to show that the two initiation methods result in quite different explosion processes. When the impactor arrives, it creates widespread plastic deformation, cracking and hot-spot generation throughout the crystal, whereas the ultrasonic hammer inputs heat to faces of the crystal (the crystal-polymer interface) by high-speed frictional rubbing. Based on these considerations, we attribute the faster rise times created by the drop hammer to the presence of initiation sites spread widely throughout the crystal interior whereas the ultrasonic hammer produces hotter initiation sites only on the crystal surface. In order to produce a crystal explosion with ultrasound, the reaction has to take time to propagate from the crystal surfaces to the crystal interior. The higher temperatures associated with ultrasound compared to drop hammer low-velocity impact seem likely to result from ultrasound inputting more heat and that heat is localized at the crystal surfaces.

The drop hammer with two simultaneous thermal imagers can measure the temperature evolution of explosives with time and space resolution sufficient to observe both the fast initial explosion and the slower combustion of material not consumed during the explosion. RDX and HMX initiation by drop hammer and ultrasonic hammer have different mechanisms which result in drop-hammer initiated explosions with faster rise times and lower temperatures than the ultrasonic hammer.

EM initiation by friction provided by ultrasound

A few years ago, the UIUC group developed a method to initiate explosives in a unique way by controlled high-speed rubbing. Explosive crystals were embedded in a polymer matrix which was pressed against an ultrasonic horn, as depicted in Fig. 16. Nothing much happened at first. This was because the ultrasonic horn hammered away at the polymer and explosive, but generally the explosive just oscillated up and down. Then we discovered if a small amount of a lubricant, either a viscous liquid such as ethylene glycol, or a slippery powder such as Teflon, was first applied to the crystal, the ultrasound would cause it to explode rapidly, with a heating rate of about 20,000K/s. The explanation is the lubricant breaks the adhesion between the crystal and polymer, which allows the crystal surfaces to rub against the polymer. The friction of rapidly rubbing the explosive surface against the polymer at 20 kHz with an amplitude of several microns was enough to produce a hot crystal/polymer interface that initiated and ignited the crystal.

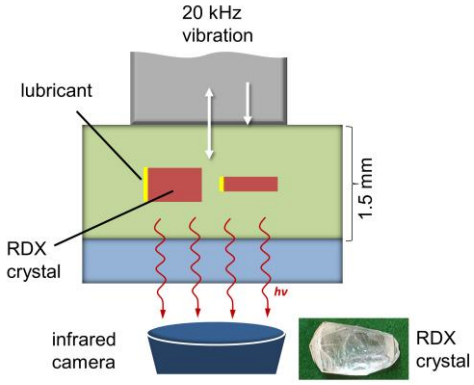

Fig. 16 Thermal histories of XTX8003 with a 2.2 km/s planar impact. The microporous XTX (red) produces 6000K hot spots at short times. The nanoporous homogenized XTX is thousands of K cooler at shorter times. When the samples are ignited, at about 50 ns, the thermal histories are about the same.

In discussions between the UIUC and USC groups we decided this was something that could be simulated, and the most interesting approach was to investigate anisotropic rubbing, i.e. rubbing crystal planar surfaces in different directions. As Fig. 16 indicates, we developed a method to do this in a controlled manner. We grew RDX crystals and used x-ray diffraction to orient them. Then one single crystal a couple of mm in dimension was cut into two pieces. The two pieces were rotated to display different crystal planes to the (up and down) motion of the acoustic hammer. We carefully lubricated one surface of the crystal to confine most of the rubbing to this surface. In this way we could compare the effects of fast rubbing a single crystal plane along different directions.

Frictional sliding of surfaces resulting in hot spots is a fundamental process that governs the ignition behavior of a wide variety of energetic material. An example is a frictional heating of RDX and HMX. While the frictional heating is believed to play an essential role for the initiation of chemical reactions in these materials, its molecular mechanisms remain largely unknown.

Cyclotrimethylene trinitramine (RDX) is sensitive to thermal and mechanical insults. A polymer binder is often used to bind and desensitize RDX. Potential initiation mechanisms in RDX include anisotropic plasticity and fracture, resulting in the decomposition of molecules. Compressive and shear dynamics models have been developed, based on reactive and nonreactive force fields, to study anisotropic shock sensitivity of RDX. Both experiments and theoretical models indicate larger sensitivity and more chemical reactivity normal to (100) and (210) planes than in other directions This anisotropy is attributed to slip systems formed by large shear stresses and steric hindrances, which increase the temperature and chemical reactivity along those directions. Understanding friction at the atomistic level is of great importance for the safe handling of HEDMs.

To understand the effect of frictional force in α-RDX, we have performed the effect of scratching surfaces on various slip and non-slip planes of α-RDX crystal by non-reactive molecular dynamics simulation. Experimental and computational studies indicate that (010) is the primary slip plane in α-RDX with [001] and [100] as slip direction as shown in Fig. 11(a).

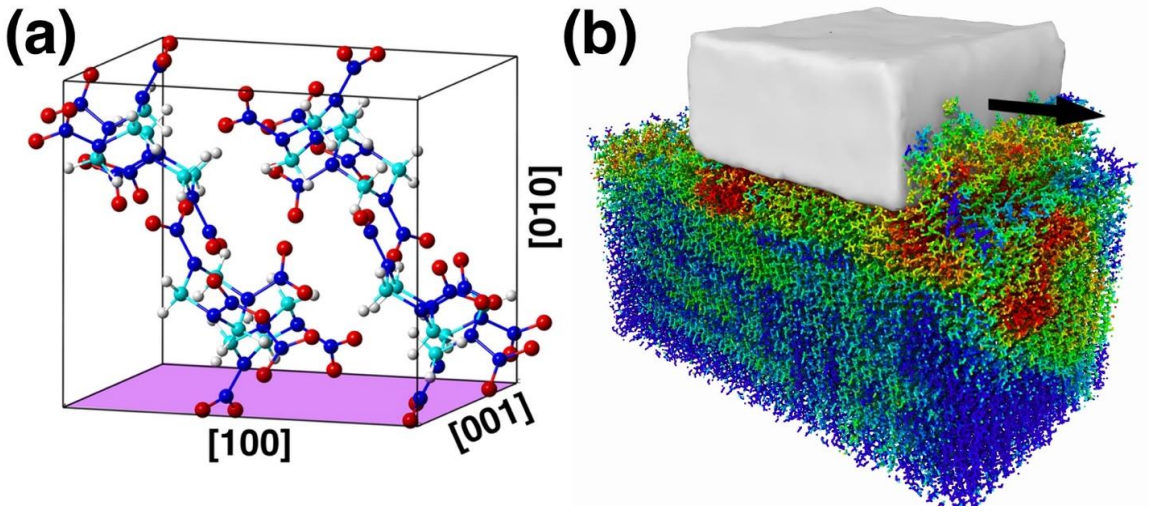

Fig. 17: (a) Crystal structure of α-RDX showing its primary slip plane. (b) Schematics of scratching simulation in α-RDX showing effect the pulling of the top block(while) on bottom RDX crystal. Black arrow shows the pulling direction. Here atoms are colored by deformation parameter, where red and green colors mean higher damaged zone.

Our scratching simulations on primary slip plane, (010), and on non-slip plane, (001) and (100), in α-RDX has shown that friction coefficient on non-slip planes are higher compared to that on slip planes. Also, the response of α-RDX crystal to scratching is different on slip and non-slip planes. While slip planes deform easily due to the nucleation of dislocations in response to applied frictional force and hence shows less heat generation in the system. But on non-slip systems, higher friction coefficient and the inability of the material to deform via dislocations results into the formation of large damaged zone and higher temperature rise inside the system. Inside this damaged zone, conformation of RDX molecules from chair to boat which is the main deformation mechanism on these non-slip planes. We also observe high spillage of RDX molecules from the surface. Figure 11(b) shows the effect of these scratching simulation in RDX crystal.

These scratching MD simulations were done using non-reactive force field developed by Smith and Bharadwaj (SB), which consists of bonding, non-bonding and Coulombic interactions. Crystal density, coefficient of linear expansion and elastic constant of RDX crystal predicted by SB potential agrees well with the experimental values. Hence it can describe the mechanical damage inside the RDX crystal during scratching simulation. Since SB potential does not allow bond breaking and bond formation, it cannot describe chemical processes in the system. To analyze the effect of chemical processes during scratching simulations, we have also performed scratching simulations on slip and non-slip planes of RDX crystal using reactive molecular dynamics simulation (ReaxFF), which allows bond breaking and bond formation. Comparison of these two force fields will help us to understand the effect of friction on RDX crystal from the perspectives of mechanical damage as well as mechanochemistry processes.

	μ (Non-Reactive)	**μ (ReaxFF)**
Slip plane: (010) [001]	0.54	0.72
Slip plane: (010) [100]	0.48	0.47
Non-slip plane: [100] [010]	0.67	0.63

Table 1: Comparison of friction coefficient (μ) computed on slip and non-slip plane using reactive and non-reactive molecular dynamics simulation

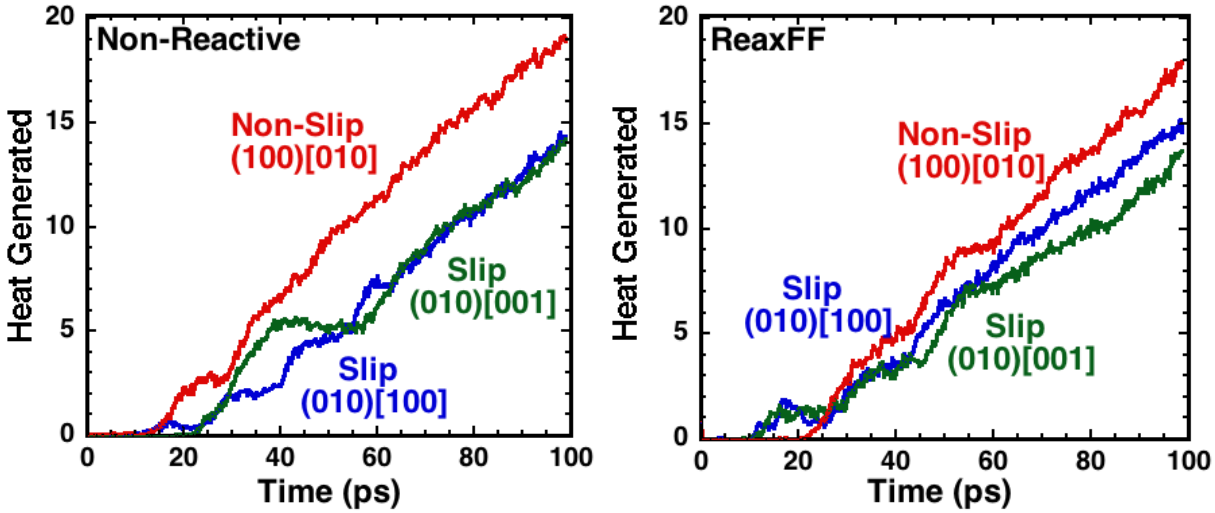

Fig. 18: Heat generated during scratching simulation. Here heat generated is equal to volume % of the system where the local temperature is greater than 100K compared to ambient temperature.

The scratching simulations are done on (010) slip plane along two different slip directions, [100] and [001], and on non-slip plane along [010] direction. Coefficient of friction computed on these planes is shown in table 2. The friction coefficient computed on these planes by non-reactive force field is also shown in table 2. It can be seen from the table that friction coefficient computed on non-slip plane (100) [010] and on slip plane (010) [100] are similar using both reactive and non-reactive force field except for the primary slip plane (010) along [001] direction. One possible reason for this is that on this slip plane RDX crystal deforms via dislocation motion as shown in our previous simulations and hence have lower friction coefficient. But ReaxFF force field is not able to describe this deformation mechanism by dislocation on (010) plane along [001] and due to which we have higher friction coefficient value here.

Figure 18 shows the comparison of temperature rise on slip and non-slip plane using reactive and non-reactive force fields. We can see that in both cases, the temperature rises on non-slip plane (100) [010] is higher than that of slip planes (010) [001] and (010) [100]. This happens mainly due to the inability of system to deform via dislocation on non-slip planes. Hence, they show formation of massive damage zones and higher temperature rise inside the system. Another important question here is the location of highest temperature rise inside the system. To locate this area, contour plots of temperature on slip and non-slip planes are calculated as a function of displacement of the scratching block, as shown in Fig. 13. It can be seen from these plots that the location of highest temperature is always near the interface between the upper and lower blocks, but its location at the interface changes as the upper block moves. Initially, the maximum temperature rise is in front of the upper block, but later its position shifts to the center of the upper block. A likely reason for having the maximum temperature at the center of the interface is because the system can readily dissipate energy near the periphery of the interfaces of the two-block compared to the center.

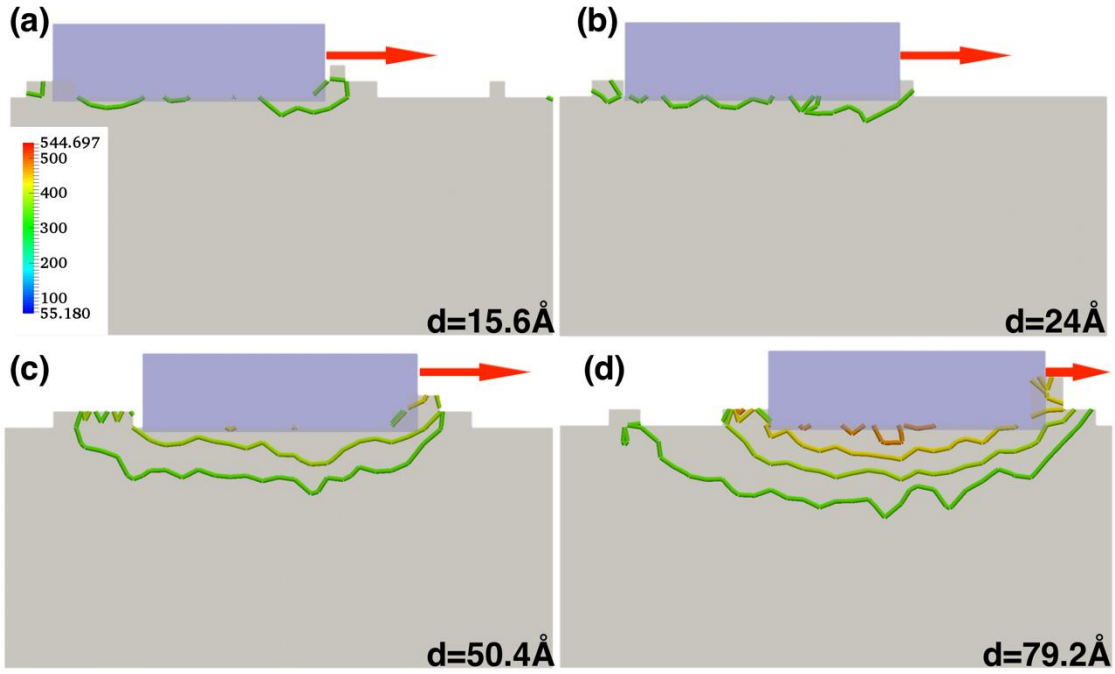

Fig. 19: Contour plots of temperature for (010) [100] frictional heating via scratching simulation for several values of displacement, d, of the upper block. Red arrows indicate the scratching direction.

To understand the effect of frictional sliding in RDX, simulations are done on slip and non-slip planes of RDX crystal. The simulation setup for frictional sliding is shown in Fig. 20. In contrast with the configuration of scratching simulation, Fig. 17b, here both the upper and the lower block have the same length. In the two simulations a, the upper block is moved at constant velocity of 40m/sec and 100m/sec on the surface of the lower block. This effect of frictional sliding of the upper block on the lower block has been monitored by observing the deformation and the temperature rise in the lower block. The periodic boundary conditions (PBC) are applied along the sliding and the width directions. These frictional sliding simulations will help us to understand deformation mechanism in polycrystalline RDX crystal like rubbing of two RDX grains against each other which we cannot study by scratching simulations.

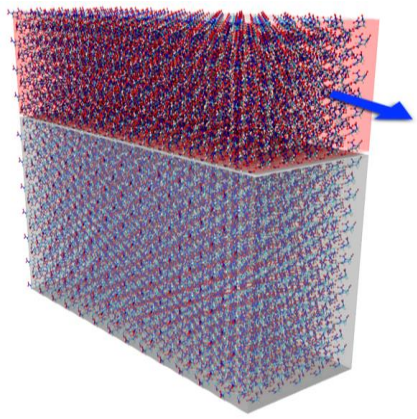

Figure 20: Schematics of the frictional sliding simulation. Here top block (shown in red) is moved at a constant velocity of either 100m/sec or 40m/sec over the surface of the lower RDX block (shown in black).

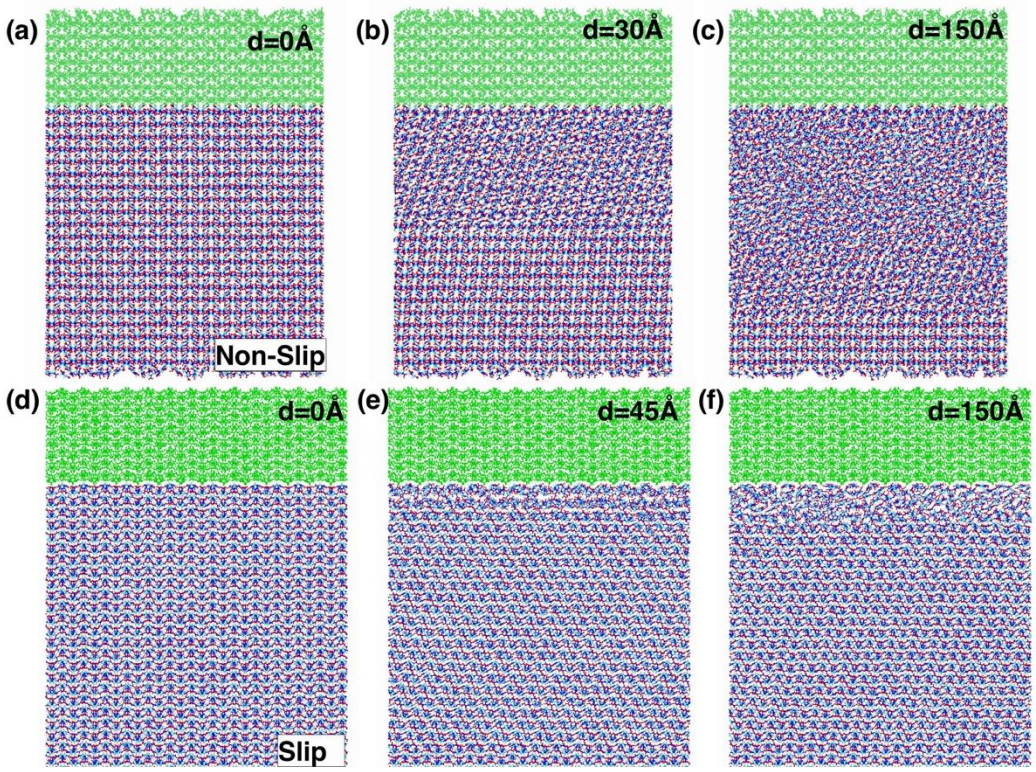

Figure 21: Effects of sliding friction on non-slip plane (100) [010] (a)-(c) and on slip plane (010) [001] (d)-(e). Here top block is shown is green color and is moved at a constant velocity of 100m/sec or 40m/sec.

Figure 21 shows the anisotropy of deformation behavior observed in RDX crystal due to the frictional sliding of RDX blocks against each other either on slip plane or on non-slip plane using non-reactive force field. Similar anisotropy in deformation behavior is observed using reactive molecular dynamics simulations. The anisotropy in the deformation pattern observed here can be explained by the earlier computed friction coefficient values on slip and non-slip plane using scratching molecular dynamics simulation. In case of non-slip plane (100), as we slide the top block (green block) along [010] sliding direction on the surface of the bottom block, we observe deformation of the bottom RDX block, figure b-c. The deformation of lower block happens here due to the high frictional force acting along the [010] direction in the lower block. Remember from our previous simulations, we have observed that (100) plane along [010] direction have maximum friction coefficient and hence frictional force is highest here. Because of this high frictional force RDX crystal deforms here layer by layer with time. Deformation of RDX layer starts at the interface of the top and bottom layer and its size grows with the displacement of top block, figure 21b,c, and finally the entire RDX crystal deforms. Also from our ReaxFF simulations, we have observed that there is no bond-breaking of RDX molecule during this deformation process and hence deformation of RDX layers happens here mainly due to the change in coordination number and conformational change of RDX molecules from chair to boat. In case of slip plane (010), a localized deformation zone forms at the interface of two blocks due to the frictional sliding along the slip direction [001]. This localized deformation zone happens here due to the low friction coefficient on the slip plane which results into low frictional

force along the sliding direction. So once a small deformation zone forms at the interface of the of the two blocks, the effect of frictional force does not propagate further inside the lower block and the size of this deformation zone remains almost constant afterward. This anisotropy in deformation pattern results into very different temperature profile inside the system as shown in Fig. 22. In case of non-slip, temperature of the entire system increases uniformly which is consistent with the layer by layer deformation of the entire RDX crystal that is observed here. In case of slip plane, the temperature rise inside the material above ambient temperature is localized near the interface of the two block which is again consistent with the localized deformation observed here.

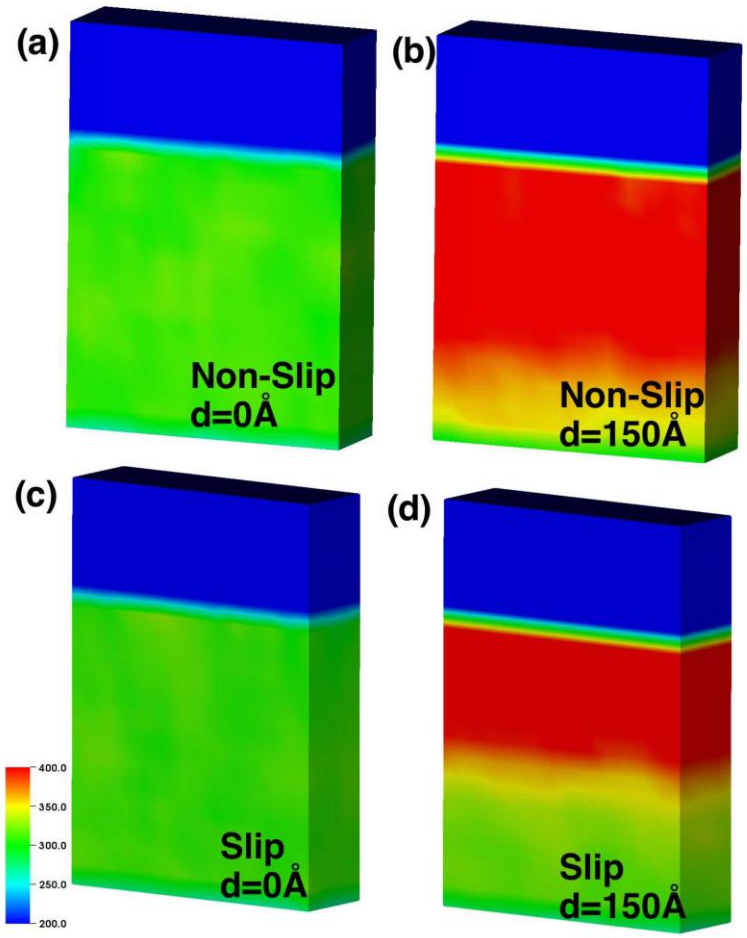

Fig. 22: Temperature profile of RDX crystal during frictional sliding on non-slip and slip plane.

Anisotropy in deformation mechanism is observed on slip and non-slip plane during both scratching and sliding friction simulation by reactive and non-reactive molecular dynamics simulation. This anisotropy in deformation mechanism happens due to higher friction coefficient on non-slip pane compared to slip plane and the ability of crystal to deform by dislocation motion on slip plane and by change in ring conformation in non-slip plane. And this anisotropy in deformation mechanism and friction coefficient results creation of hot spots and into higher temperature rise on non-slip plane compared to slip plane.

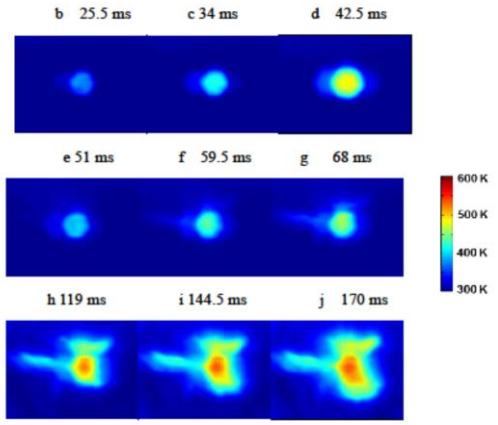

Fig. 23 high-speed thermal image movie of a single α-RDX crystal surrounded by PDMS binder exploding due to high-speed rubbing.

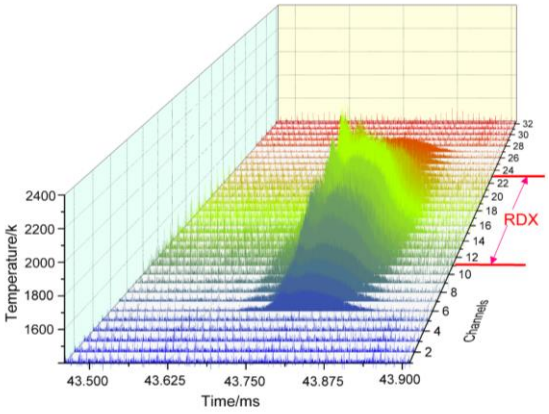

Fig. 24 Much faster thermal images of an RDX crystal exploding, obtained using the linear array.

For the experiments, we start by looking at what happens with a single RDX crystal being rubbed along all its surfaces (lubricant applied on the entire crystal). A movie of thermal images is shown in Fig. 23. The thermal imaging camera takes one frame every 8.3 ms. The crystal stays intact and heats up. At about 119 ms it is seen to explode and jet hot gas all over the place. The peak temperature was about 600K. We can't really see when the crystal explodes because the explosion is a fast event that occurs between frames. To deal with this problem, we developed a unique fast event thermal imaging system. It consists of 32 high-speed (>1 μs) thermal detectors in a linear array. Because we reduced the number of pixels that need to be read out, and increased the number of A/D converters, we can read out the linear array much faster. However we don't get a 2D movie but rather a 1D line scan through the crystal. The result is shown in Fig. 24. The crystal in this case blew up at about 44 ms, and the explosion lasted less than 0.1 ms.

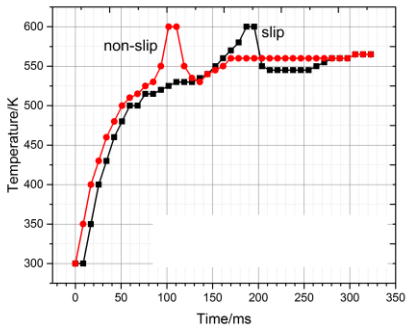

Fig. 25. Results of anisotropic rubbing of RDX crystal. When rubbed along the [001] direction, the non-slip direction makes the crystal explode much faster.

In the rubbing experiments, to conform with USC simulations, the UIUC group always rubbed the α-RDX crystal along the [001] direction, but with different rotation angles around the [001] plane normal. As shown in Fig. 25 where we rubbed pieces of the same crystal along the slip and non-slip [001] direction, rubbing along the non-slip direction caused the crystal to explode 100 ms faster than rubbing along the slip direction. Interestingly, rubbing along the non-slit direction also causes the explosion to start faster. This result along with others not shown generally confirms the USC group prediction.

Initiation by high-speed impact

Our shock compression microscope is depicted in Fig. 26. There is a laser flyer launcher array[16-18] and a shock target array. The sample is viewed through a sacrificial glass witness plate and a microscope objective. There is a photon Doppler velocimeter (PDV)[19,20] to determine velocities, densities, energies and pressures, and an optical pyrometer[13] to measure time-dependent temperatures above 2000K. We have nanosecond and femtosecond lasers for strobe photography,[16] ultrafast spectroscopy[21,22] and excitation of photoemissive probes[23-27] in the samples. Although it won't be discussed in this proposal, there are actually two microscopes. The second is set up for femtosecond infrared reflection absorption spectroscopy (fs RAIRS) and it uses femtosecond IR pulses tunable from 2.5 to 12 μm. We can get quite good single-shot spectra of vibrational transitions of PBX samples.

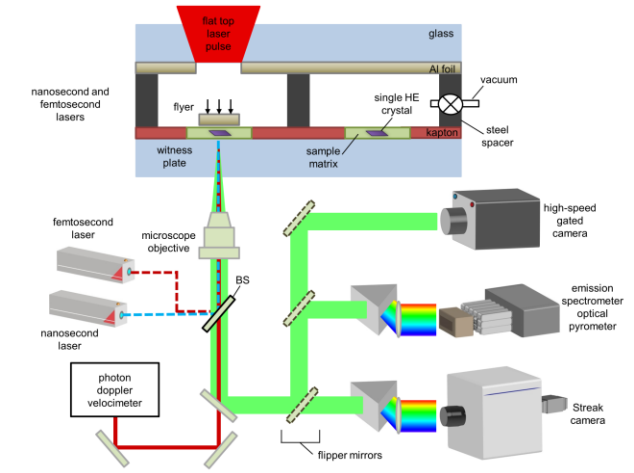

Fig. 26. Shock compression microscope.

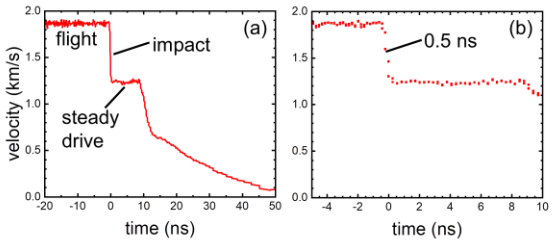

Fig. 27. Photon Doppler velocimetry (PDV) of a 50 μm thick Al flyer hitting a glass window at 1.88 km/s at time = 0. Note the steadiness of the flight through vacuum at t < 0, the suddenness of the impact at t = 0 and the 8 ns of steady shock drive at t > 0. The shock risetime was < 0.5 ns.

People have used laser-launched flyer plates for about 50 years, and there are always concerns about whether the flyer is flat, melted, vaporized and in a stage of disintegration. We have turned laser flyer plates into a precision scientific tool.[16] We have arranged the geometries so we are always in a planar shock geometry, at least for run distances up to about 250 μm. We usually use Al foil for the flyers. Other metal foils work but do not seem to have any particular advantage. Flyer velocities can range from 0-6 km/s, and the flyer thickness from 12-100 μm, which produces shocks of durations ranging from 2 to 16 ns.[16,18] Figure 27 is an example of the precision of the flyer plate impact. It is a PDV of a 50 μm thick Al flyer hitting a borosilicate glass window at 1.87 km/s. In Fig. 27a, note the stable free flight through vacuum at t < 0, the sudden impact and the very flat region of steady drive lasting 8 ns indicative of a planar shock. Figure 27b shows the impact. The rise time of the impact is no more than 0.5 ns.

Some optical pyrometry results are shown in Fig. 28, obtained from four different plastic-bonded explosives (PBX) made in our labs, containing PETN, RDX, TNT and TATB. The PBX charges were impacted at 2.9 km/s. These are the average of 25 shots, and the error bars reflect the fact that each PBX charge has a unique microstructure. The higher temperatures at shorter times are due to hot spots. At longer times we get the normal combustion temperature of these explosives. RDX has a slower process that shifts the temperature maximum out to about 40 ns. TNT and TATB are noticeably colder.

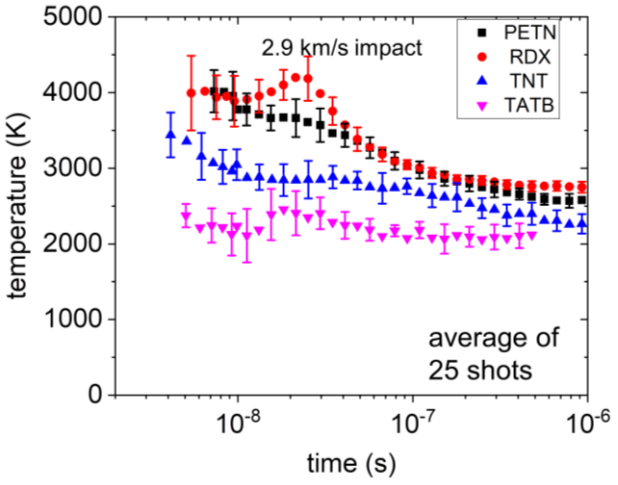

Fig. 28. Temperature histories from four plastic-bonded explosives (PBX) impacted at 2.9 km/s. These are the average of 25 shots and the error bars reflect heterogeneity among the different explosive charges.

We subjected the XTX8003 and simulant samples to km/s planar impacts with flyer plates. The thermal history of the shocked explosives was studied using high dynamic range optical pyrometry. Experiments were done with more than 1,000 shots under a variety of different conditions. The first batch of PBX we produced had a large concentration of micropores. We found that we could homogenize the PBX by running it through a hydraulic press. After homogenization there were zero pores bigger than 1 mm but there presumably were nanopores we could not see with SEM or CT scanning.

Figure 29 shows a typical optical pyrometer output for XTX8003 that was either microporous or homogenized nanoporous at an impact speed of 2.2 km/s. The figure shows that the thermal histories of the two types of materials are similar after about 50 ns, but during shorter times the microporous XTX is far hotter, 6000K versus 4000K. This result is indicative of the formation of 6000K hot spots at short times after impact in the microporous material.

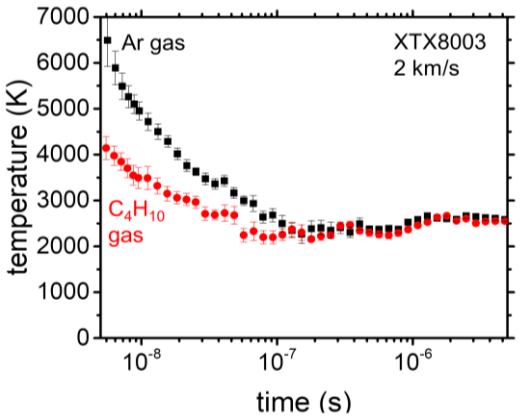

Fig. 29 *Changing nothing but the gas in the pores has a dramatic effect on the hot spot temperatures showing that the hot spots are due to gas compression in the pores. The temperature of the hot spots decreases dramatically with higher heat capacity butane gas fill.*

By exposing the samples to vacuum and backfilling with various gases, we showed that the hot spots in the microporous XTX resulted from compression of gas in the micropores. The hot spot temperature will be higher when said gas has a lower heat capacity, and lower when the gas has a higher heat capacity. Figure 30 compares XTX8003 where the pores are filled with

low-heat capacity monatomic Ar gas to higher-heat capacity polyatomic (14-atom) butane. Changing nothing but the pore fill gas, the hot spot temperatures dropped by thousands of K.

Now we have a bit of a conundrum. The photography results on polymer-encased crystals showed hot spots in the solid material but the pyrometry shows hot spots in gas-filled voids. Which is right? The answer, we believe is both. The hot spots in solids are generally 2500-3000K whereas the void collapse is producing 4000-4500K. Due to the Planck blackbody equation, the intensity of thermal emission is (integrated over all wavelengths) proportional to T^4. We use a limited set of wavelengths, and simulations we performed indicate that in this temperature range, the dependence is more like $T^{4\text{-}5}$. This may be another way of saying that in pyrometry measurements where the sample has a distribution of temperatures, the pyrometer is primarily sensitive to the hottest part. So the hot gas in the nanopores overwhelms the pyrometry signal.

What is happening in the pores is not explained in detail by the experiments. Certainly the gas is compressing and getting very hot, but this is neither adiabatic nor nonreactive. The gas is in a pore surrounded by reactive explosive material. The pore collapse will involve numerous mechanical instabilities due to the complex structure of the surrounding explosive and binder. The explosive is being heated to a lesser extent by plastic deformation, and there will be violent thermal energy transfer events which erode and volatilize the explosive. These effects are therefore being investigated using atomistic simulations. The initial simulations used a simplified model system.

The USC group performed multi-million molecular dynamics simulation of shock compression on porous silica glass to obtain atomistic insights of how gas particles confined within a small pore heat up under shock compression. To estimate the extent of gas heat up as a function of the initial gas particle density D_{initial}., we performed a series of shock compression simulations of argon atoms using Lennard-Jones (L-J) potential. Starting from various initial gas densities in the pore, we thermalize the gas particles at 300K and then shock compresses the system.

Figure 30 shows a center-cut view of the simulation setup. The system dimensions are $57.28\times57.28\times65.0$ nm^3. The porous silica matrix is obtained with the melt-quench procedure. To examine the effect of porosity in the shock-induced gas heating, we have created two silica matrices with different porosity, *i.e.*, the void-to-system volume ratios $V_{\text{void}}/V_{\text{system}}$

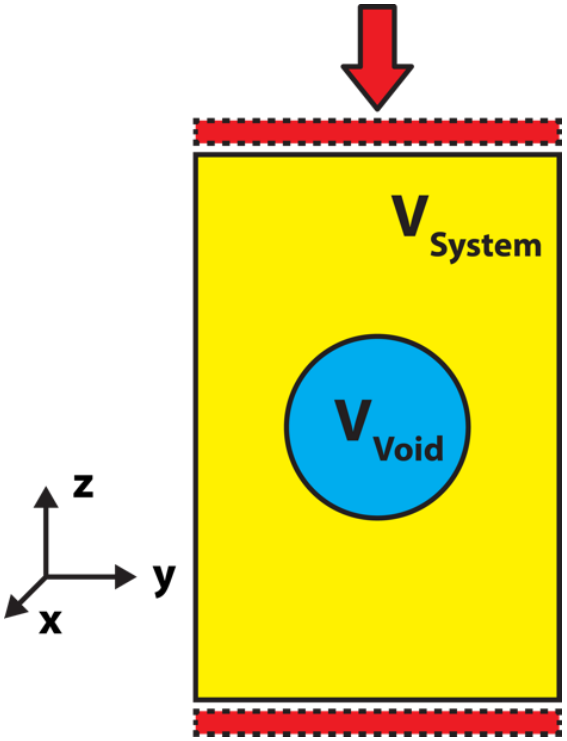

Fig. 30: A center-cut view of the simulation setup. The yellow rectangle and the light blue circle represent the silica matrix and a spherical void at the center of the system respectively. Two red rectangles at the top and bottom of the system indicate the locations of imaginary walls with repulsive interaction. The top wall moves at the particle velocity V_p in the negative z-direction to apply a shock.

are 3% and 6%. These systems are compressed up to prescribed strains, 2% and 5% respectively. The total number of atoms and the number of L-J atoms in the two systems are given in Table 2. A planar shock is induced along the z-axis by the momentum-mirror technique. Two particle velocities V_p = 1 km/s and 3 km/s are examined in this study.

Table 2: System porosity, total number of atoms, number of L-J particle.

V_{void}/V_{system} Ratio	Total Number of Atoms	Number of Gas atoms
3%	13,093,430	9,658
6%	12,682,098	19,658

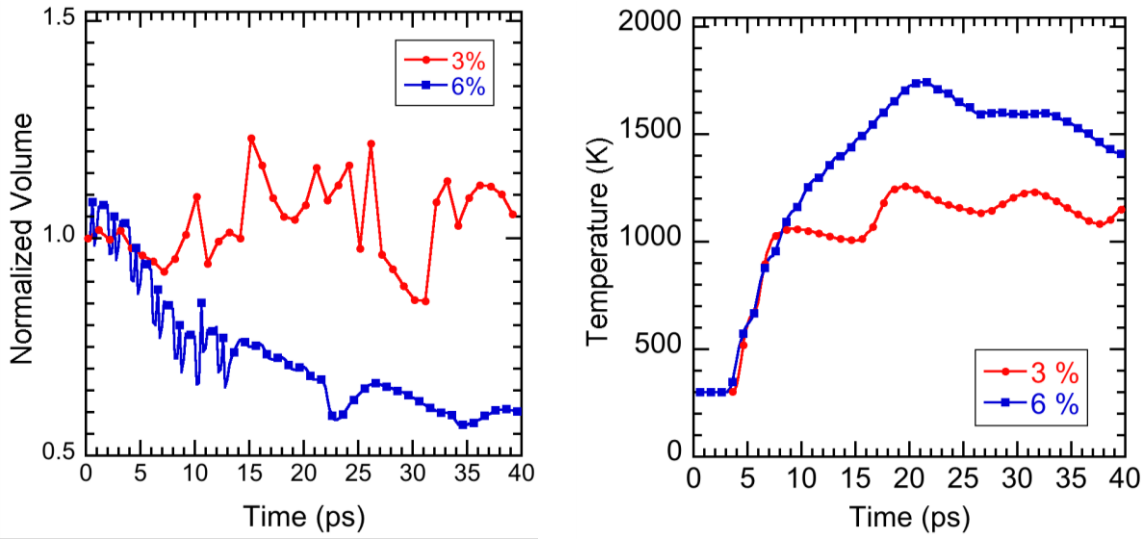

Fig. 31: Profile of void volume (left) and temperature of gas particle (right) with particle velocity 1km/s in the systems with 3% (red) and 6% (blue) porosity.

Figure 31 shows the time evolution of the void volume (left) and the temperature of gas particle (right) in the 3% and 6% porosity systems subjected to a shock of V_p = 1km/s. We found that distinct shock responses of the void in these simulations. With 6% porosity, the void volume monotonically decreases to 60% of the original size in 40ps. On the other hand, the void shows almost no shrinkage in volume and oscillates with 3% porosity. The temperature of the gas particles rapidly increases in both systems; the peaks in temperature at 1233.7K at 31.4ps with 3% porosity and 1743.0K at 20.8ps with 6% porosity are observed.

We have also performed shock compression simulations with V_p = 3km/s to study the effect of shock speed. Figure 32 shows the void volume profile in the systems with 3% and 6% porosity. With 3% porosity, the volume of the void decreases to and oscillates around 80% of the original size. With 6% porosity, the void has completely collapsed into 5% of original volume in 50ps.

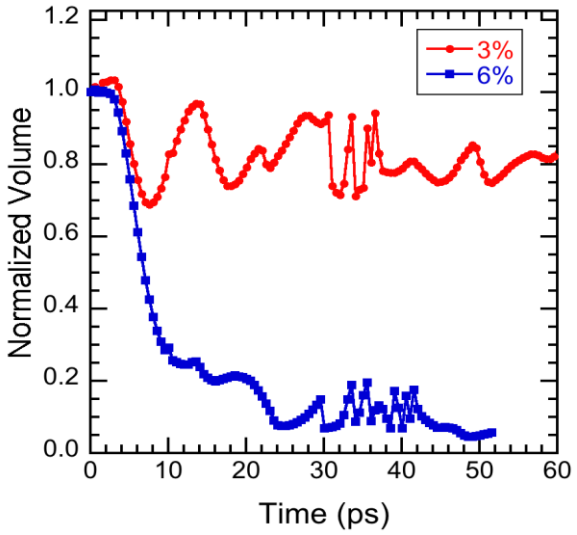

Fig. 32: Void volume profile with 3% and 6% porosity subjected to a shock at V_p = 3km/s.

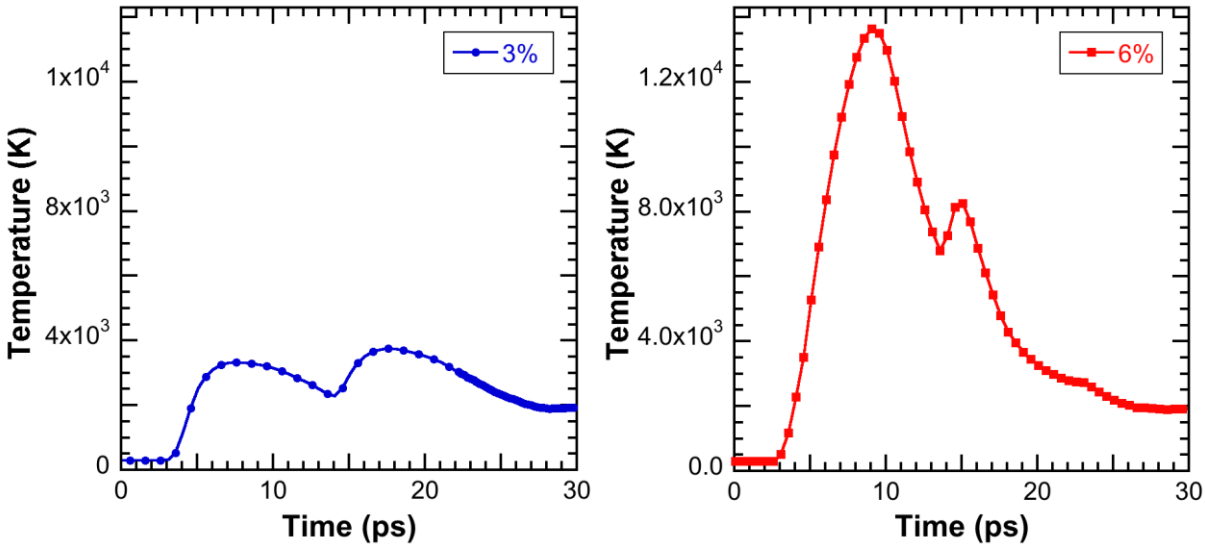

Fig. 33: Temperature profile of gas particles with 3% (left) and 6% (right) porosity.

With V_p = 3km/s, the temperature of gas particles rapidly increases at the arrival of the shock wave. Figure 33 shows that the peak temperatures we obtain are 3,745K at 17.6ps with 3% porosity and 13,628K at 9.1ps with 6% porosity, respectively. Experimentally observed hot spot temperature was 6,000K in a PETN-based sample with micropores at 2.8km/s.

Though the transient temperatures in simulation appear extremely high compare to the experiment it is noteworthy that by averaging the temperature of gas particles over 30ps we have obtained the gas temperature at 2,380K with 3% porosity and 5,163K with 6% porosity, respectively.

To highlight the effect of the nonreactive gas particles in the hotspot formation, we have performed a pair of shock simulations with same initial conditions except whether the void is filled with gas molecules with Lennard-Jones potentials or empty. Planar shock is induced by the momentum mirror technique, in which a planar repulsive wall at a constant velocity moves through the system. A higher average temperature rise of the system is observed with the gas-filled void. Though hotspot formation is observed in the two simulations, our simulation shows a sustained hotspot presence with the gas-filled void while transient and rapid decreases of elevated temperature is found with the empty void. To further analyze the difference between the filled and empty case at various particle velocities we have performed fragment analysis to analyze the formation of various clusters in the system. Figure 34 presents the time evolutions of molecular fragments at lowest and highest particle velocities of 2 and 4 km/s.

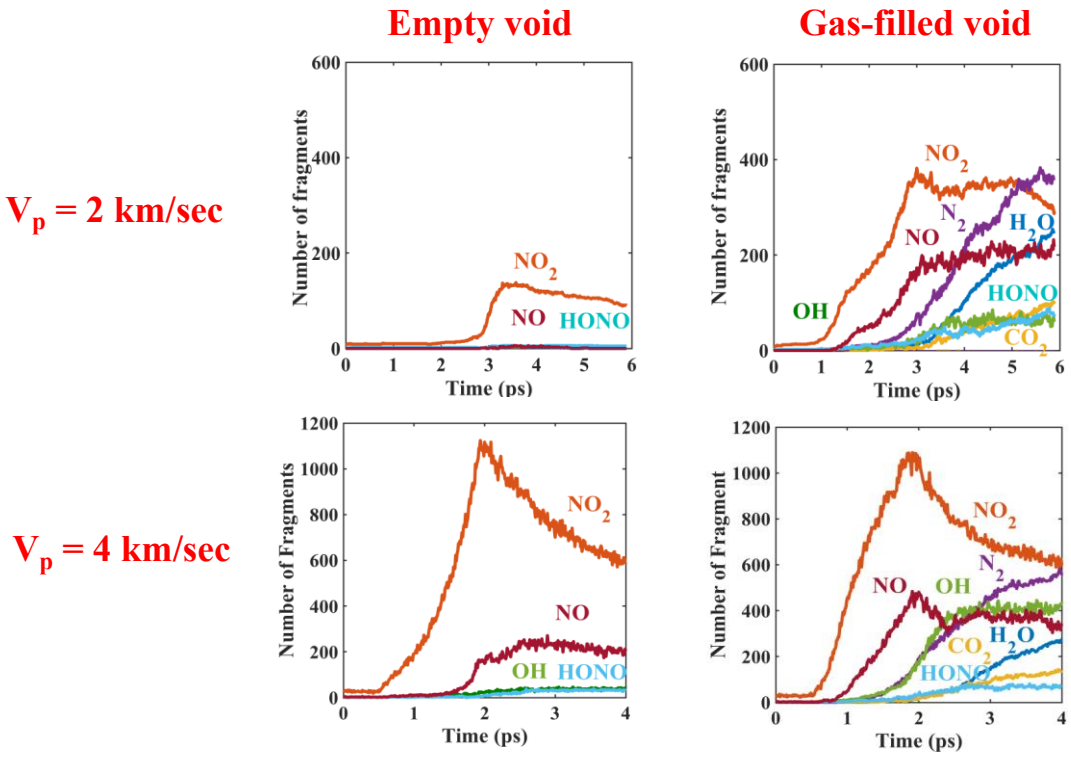

Figure 34: *Fragment formation at higher V_p is considerably higher as compared to the lower particle velocities. In empty void case only NO_2 formation is noticeable while many fragments are formed in filled void case at different V_p.*

The large numbers and variety of molecular fragments are found at V_p = 4 km/s while a few fragments such as NO and NO_2 are observed at V_p = 2 km/s. The formation of NO_2 fragments decreases when the void has completely collapsed in these systems, indicating further reactions between of NO_2 and RDX molecules under the high pressure and temperature environment.

We have been able to produce well-characterized detonations in homogeneous liquid explosives and in PBX. A detonation is a shock wave sustained by heat and pressure-generating chemical reactions.[28] A steady detonation, to an observer moving at the detonation velocity, is one where the structure of the reaction zone appears unchanging in time.[29] But inside this nominally unchanging reaction zone, the microstructure and the molecules are highly active. Usually, shock-to-detonation experiments take microseconds and millimeters of sample length. Taking so long to develop the detonation means it is difficult to see the fast processes happening in the reaction zone, which occur in picoseconds to tens of nanoseconds.[30-32] We have developed the ability to produce well-characterized detonations in liquid[11] and solid explosives starting from a short-duration input shock pulse of the correct input pressure. The correct pressure seems to be a little bit bigger than the von Neumann spike pressure at the leading edge of the detonation front. By starting with a short pulse, we make a thin von Neumann spike which spreads out and creates a detonation. By using a short pulse and getting into detonation as quickly as possible, we are in the best position to time resolve the detonation front.

Figure 35 shows data from shocked nitromethane (NM).[11] Figure 35 shows how the input shock, which is nominally a 4 ns rectangle with an input pressure of 18 GPa, produced by a 4 km/s impact with a 25 μm thick Al flyer, propagates through NM. The pressures were computed from PDV velocity measurements using the NM Hugoniot from the literature[33] along with our measurements. Recall our geometry is such that the shock remains planar longer than the longest run distance, which here was 210 μm. About 8 ns after the shock enters NM, there is a big volume explosion and the 18 GPa pressure briefly jets up to about 35 GPa. After the volume explosion, things settle down and a triangular shock that is about 11 ns in duration is formed. That shock maintains a constant profile until the end of the experiment.

Figures 35b and 35c show the detonation velocity, von Neumann spike pressure, Chapman-Jouguet pressure, and reaction zone length and duration. All these parameters agree with previously published studies on bomb-sized charges of NM. Our Hugoniot agrees with more than one previous study.[33,34] The NM detonation velocity from an explosives handbook was 6.29 km/s compared with our 6.2 km/s.[35] Measurements of the CJ pressure were discussed in Menikoff and Shaw,[36] where the CJ pressure was calculated to be 10.34 GPa. Other calculations with CHEETAH software codes gave 11.4-13.2 GPa.[37] Dattelbaum and co-workers gave the CJ pressure as 12.5 GPa.[38] We obtained 11.2 GPa. The VNS pressure has been computed and measured in various ways. Menikoff and Shaw calculated it to be 21.1 GPa[36] and

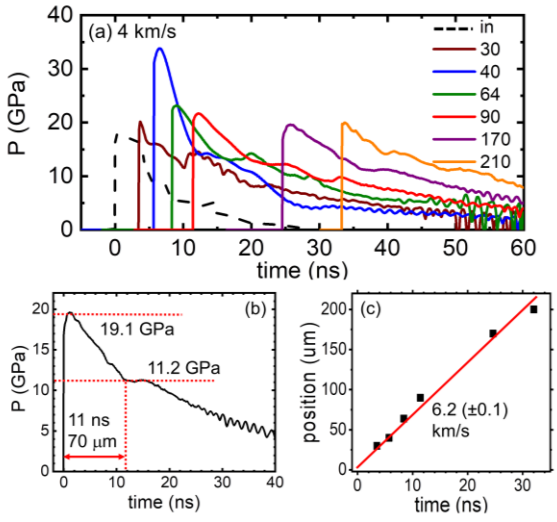

Fig. 35. Propagation of a 4 ns 18 GPa shock through nitromethane (NM) measured by PDV. After about 8 ns the NM explodes and the explosion decays into a steadily-running chemically-sustained shock, i. e. a detonation. (b) The von Neumann spike pressure, the Chapman Jouguet pressure and the reaction zone length. (c) The detonation velocity.

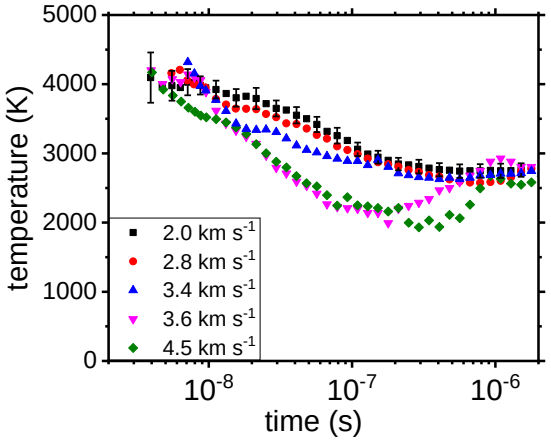

Fig. 36. Temperature histories of XTX-8003 at different impact velocities. After a brief initial hot spot period the sample cools thousands of K via adiabatic expansion. There are two distinct types of cooling, with the much faster one happening above 3.2 km/s.

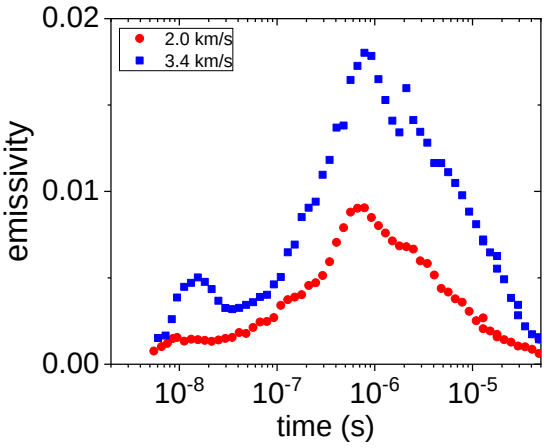

Fig. 37. Time-dependent emissivities of XTX-8003 with 2.0 km/s and 3.4 km/s shocks in the slower and faster cooling regimes, respectively. The emissivities are proportional to the hot spot density.

Partom calculated it to be 19.1 GPa,[39] compared to our 19.1 GPa. The reaction zone width was deduced to be 36 μm by Engelke and co-workers[40] and calculated to be 11 μm by Menkioff and Shaw,[36] compared to our 11 μm. Pyrometry by Yoo and co-workers gave a detonation temperature of 3600K,[41-43] which was the same as obtained by Bouyer and co-workers.[37,44] We obtained 3430 (±240)K.

What we see here is a shock that is chemically sustained, which maintains a constant profile as it propagates until the end of the experiment. Its properties are exactly what we know from many years of NM detonation studies. The diameter of the shocked region, 0.5 mm, is less than the 2.5 mm critical diameter of NM, so this shock would not be able to propagate indefinitely, but it maintains planarity through the duration of the experiment, until the NM is exhausted. It is a detonation on a tabletop.

In studies of XTX-8003, we obtained the temperature and emissivity histories in Figs. 36 and 37. The temperature profiles in Fig. 36 consist of a brief constant hot spot temperature followed by a cooling phase. The cooling occurs via adiabatic expansion, and the cooling dramatically speeds up around 3.2 km/s. The emissivities in Fig. 37 represent volume fractions of hot spots, which are small. Figure 38 shows shock propagation through a PBX charge with an impact velocity in the slower or faster cooling regime. Figure 38 shows the slower cooling occurs when the shock is underdriven and the faster cooling occurs when the shock is overdriven. Figure 39 combines the temperature histories and high-speed microscope video in both regimes. Looking back at Fig. 37, we see that the hot spot population grows over the first 10 ns or so. This time is determined by shock propagation through the sample. After the generation period there is a constant period where supercritical hot spot growth is countered by the death of subcritical hot spots. After the subcritical hot spots die out, there is a rapid growth of the supercritical hot spots until the entire sample is aflame.

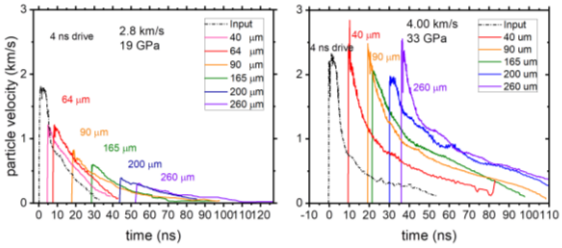

Fig. 38. *Propagation of a 4 ns shock through a PBX charge of XTX8003 made from PETN and PDMS. (a) A 19 GPa input decays away. (b) A 33 GPa input generates a steadily-running chemically-sustained shock.*

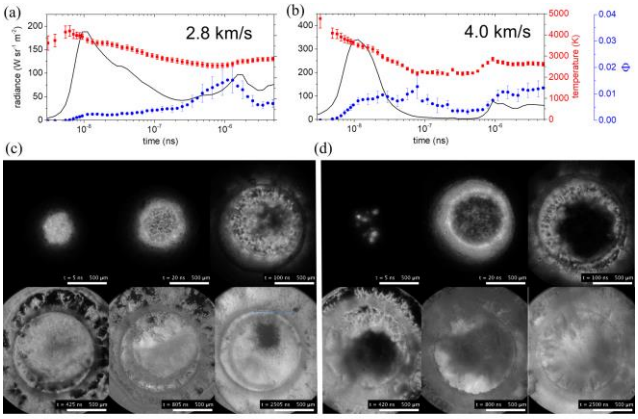

Fig. 39. *Temperature histories and videos reassembled from multiple shots for XTX8003. The 2.8 km/s impact produces a decaying shock and the 4.0 km/s impact produces a detonation. The expanding gas is the dark circle, which is colder than the surrounding reacting solid.*

Concluding remarks

During this 3 year project, the UIUC and USC teams collaborated to understand the effects of microstructure on energetic material initiation. They developed instruments to study initiation by ultrasound, low velocity and high velocity impacts, that provided high spatial and temporal resolution of temperature, pressure, density, composition and microstructure. Nonreactive and reactive atomistic simulations were performed to understand the ultrasound and high velocity impact experiments at a fundamental molecular level. The authors of this report wish to express their appreciation to AFOSR for support of this project.

Literature cited

1. Z. Men, W. P. Bassett, K. S. Suslick, and D. D. Dlott, Drop hammer with high-speed thermal imaging, *Rev. Sci. Instrumen.* **89**, 115104 (2018).
2. Z. Men, K. S. Suslick, and D. D. Dlott, Thermal explosions of polymer-bonded explosives with high time and space resolution, *J. Phys. Chem. C.* **122**, 14289–14295 (2018).
3. M.-W. Chen, S. You, K. S. Suslick, and D. D. Dlott, Hot spots in energetic materials generated by infrared and ultrasound, detected by thermal imaging microscopy, *Rev. Sci. Instrum.* **85**, 023705 (2014).
4. M.-W. Chen, S. You, K. S. Suslick, and D. D. Dlott, Hot spot generation in energetic materials created by long-wavelength infrared radiation, *Appl. Phys. Lett.* **104**, 061907 (2014).
5. S. You, M.-W. Chen, D. D. Dlott, and K. S. Suslick, Ultrasonic hammer produces hot spots in solids, *Nature Commun.* **6**, 6581 (2014).
6. P. Rajak, A. Mishra, C. Sheng, S. Tiwari, R. K. Kalia, A. Nakano, and P. Vashishta, Anisotropic frictional heating and defect generation in cyclotrimethylene-trinitramine molecular crystals, *Applied Physics Letters* **112**, 211604 (2018).
7. D. D. Dlott, Shock compression dynamics under a microscope, *AIP Confer. Proc.* **1793**, 020001 (2017).

8. W. P. Bassett and D. D. Dlott, High dynamic range emission measurements of shocked energetic materials: Octahydro-1,3,5,7-tetranitro-1,3,5,7-tetrazocine (HMX), *J. Appl. Phys* **119**, 225103 (2016).
9. W. P. Bassett and D. D. Dlott, Shock initiation of explosives: Temperature spikes and growth spurts, *Appl. Phys. Lett.* **109**, 091903 (2016).
10. W. P. Bassett, B. P. Johnson, N. K. Neelakantan, K. S. Suslick, and D. D. Dlott, Shock initiation of explosives: High temperature hot spots explained, *Appl. Phys. Lett* **111**, 061902 (2017).
11. M. Bhowmick, E. J. Nissen, and D. D. Dlott, Detonation on a tabletop: Nitromethane with high time and space resolution, *J. Appl. Phys.* **124**, 075901 (2018).
12. D. Stirpe, J. O. Johnson, and J. Wackerle, Shock initiation of XTX-8003 and pressed PETN, *J. Appl. Phys* **41**, 3884-3893 (1970).
13. W. P. Bassett and D. D. Dlott, Multichannel emission spectrometer for high dynamic range optical pyrometry of shock-driven materials, *Rev. Sci. Instrum.* **87**, 103107 (2016).
14. C. S. Coffey and V. F. De Vost, Impact testing of explosives and propellants, *Propell. Explos. Pyrotech.* **20**, 105-115 (1995).
15. D. M. Williamson, S. Gymer, N. E. Taylor, S. M. Walley, A. P. Jardine, A. Glauser, S. French, and S. Wortley, Characterisation of the impact response of energetic materials: observation of a low-level reaction in 2,6-diamino-3,5-dinitropyrazine-1-oxide (LLM-105), *RSC Advances* **6**, 27896-27900 (2016).
16. A. A. Banishev, W. L. Shaw, W. P. Bassett, and D. D. Dlott, High-speed laser-launched flyer impacts studied with ultrafast photography and velocimetry, *J. Dyn. Behav. Mater.* **2**, 194-206 (2016).
17. K. E. Brown, W. L. Shaw, X. Zheng, and D. D. Dlott, Simplified laser-driven flyer plates for shock compression science, *Rev. Sci. Instrum.* **83**, 103901 (2012).
18. A. D. Curtis, A. A. Banishev, W. L. Shaw, and D. D. Dlott, Laser-driven flyer plates for shock compression science: Launch and target impact probed by photon Doppler velocimetry, *Rev. Sci. Instrum.* **85**, 043908 (2014).
19. A. D. Curtis and D. D. Dlott, Dynamics of shocks in laser-launched flyer plates probed by photon Doppler velocimetry, *J. Phys.: Conf. Ser.* **500**, 192002 (2014).
20. J. Weng, X. X. Wang, Y. Ma, H. Tan, L. Cai, J. Li, and C. Liu, A compact all-fiber displacement interferometer for measuring the foil velocity driven by laser, *Rev. Sci. Instrum.* **79**, 113101 (2008).
21. W.-L. Liu, W. P. Bassett, J. M. Christensen, and D. D. Dlott, Emission lifetimes of a fluorescent dye under shock compression, *J. Phys. Chem. A* **119**, 10910–10916 (2015).
22. X. Zhou, L. Li, D. D. Dlott, and O. V. Prezhdo, Molecular photophysics under shock compression: Ab initio nonadiabatic molecular dynamics of Rhodamine dye, *J. Phys Chem. C* **122**, 13600-13607 (2018).
23. A. A. Banishev and D. D. Dlott, Ultrafast pressure-sensitive paint for shock compression spectroscopy, *J. Appl. Phys.* **115**, 203515 (2014).
24. A. A. Banishev, W. L. Shaw, and D. D. Dlott, Dynamics of polymer response to nanosecond shock compression, *Appl. Phys. Lett.* **104**, 101914 (2014).
25. J. M. Christensen, A. A. Banishev, and D. D. Dlott, Bright emissive core-shell spherical microparticles for shock compression spectroscopy, *J. Appl. Phys.* **116**, 033513 (2014).
26. Z. Kang, A. A. Banishev, G. W. Lee, D. A. Scripka, J. Breidenich, P. Xiao, J. Christensen, M. Zhou, C. J. Summers, D. D. Dlott, and N. N. Thadhani, Exploration of CdTe quantum dots as

mesoscale pressure sensors via time-resolved shock-compression photoluminescent emission spectroscopy, *J. Appl. Phys* **120**, 043107 (2016).
27. P. Xiao, Z. Kang, A. A. Banishev, J. Breidenich, D. A. Scripka, J. M. Christensen, C. J. Summers, D. D. Dlott, N. N. Thadhani, and M. Zhou, Laser-excited optical emission response of CdTe quantum dot/polymer nanocomposite under shock compression, *Appl. Phys. Lett.* **108**, 011908 (2016).
28. W. Fickett and W. C. Davis, *Detonation*, University of California Press, Berkeley, CA, 1979.
29. R. Engelke and J. B. Bdzil, A study of the steady-state reaction zone structure of a homogeneous and a heterogeneous explosive, *Phys. Fluids* **26**, 1210-1221 (1983).
30. C. M. Tarver, J. W. Forbes, and P. A. Urtiew, Nonequilibrium Zeldovich-Von Neumann-Doring theory and reactive flow modeling of detonation, *Russ. J. Phys. Chem. B* **1**, 39-45 (2007).
31. C. M. Tarver, Multiple roles of highly vibrationally excited molecules in the reaction zones of detonation waves, *J. Phys. Chem. A* **101**, 4845-4851 (1997).
32. D. D. Dlott, New developments in the physical chemistry of shock compression, *Annu. Rev. Phys. Chem.* **62**, 575-597 (2011).
33. S. P. Marsh, *LASL Shock Hugoniot Data*, University of California Press, Berkeley, CA, 1980.
34. K. E. Brown, S. D. McGrane, C. A. Bolme, and D. S. Moore, Ultrafast chemical reactions in shocked nitromethane probed with dynamic ellipsometry and transient absorption spectroscopy, *J. Phys. Chem. A* **118**, 2559-2567 (2014).
35. J. Köhler and R. Meyer, *Explosives, fourth edition*, VCH Publishers, New York, 1993.
36. R. Menikoff and M. S. Shaw, Modeling detonation waves in nitromethane, *Combust. Flame* **158**, 2549-2558 (2011).
37. V. Bouyer, I. Darbord, P. Hervé, G. Baudin, C. Le Gallic, F. Clément, and G. Chavent, Shock-to-detonation transition of nitromethane: Time-resolved emission spectroscopy measurements, *Combust. Flame* **144**, 139-150 (2006).
38. D. M. Dattelbaum, S. A. Sheffield, D. B. Stahl, and A. M. Dattelbaum, Influence of hot spot features on the shock initiation of heterogeneous nitromethane, *AIP Confer. Proc.* **1195**, 263-266 (2009).
39. Y. Partom, Revisiting shock initiation modeling of homogeneous explosives, *J. Energ. Mater.* **31**, 127-142 (2013).
40. R. Engelke, S. A. Sheffield, H. L. Stacy, and J. P. Quintana, Reduction of detonating liquid nitromethane's chemical reaction-zone length by chemical sensitization, *Phys. Fluids* **17**, 096102 (2005).
41. C. S. Yoo and N. C. Holmes, Shock initiation of nitromethane, *AIP Conf. Proc.* **309**, 1567-1570 (1994).
42. C. S. Yoo, N. C. Holmes, and P. C. Souers, Time-resolved temperatures of shocked and detonating energetic materials, *AIP Conf. Proc.* **370**, 913-916 (1996).
43. C. S. Yoo, N. C. Holmes, and P. D. Souers, "Detonation in shocked homogeneous high explosives," in *Decomposition, Combustion, and Detonation Chemistry of Energetic Materials*, edited by T. B. Brill, T. P. Russell, W. C. Tao, and R. B. Wardle (Materials Research Society, Pittsburgh, 1996), Vol. 418, pp. 397-406.
44. V. Bouyer, G. Baudin, C. Le Gallic, and P. Herve, Emission spectroscopy applied to shock to detonation transition in nitromethane, *AIP Conf. Proc.* **620**, 1223-1226 (2002).